



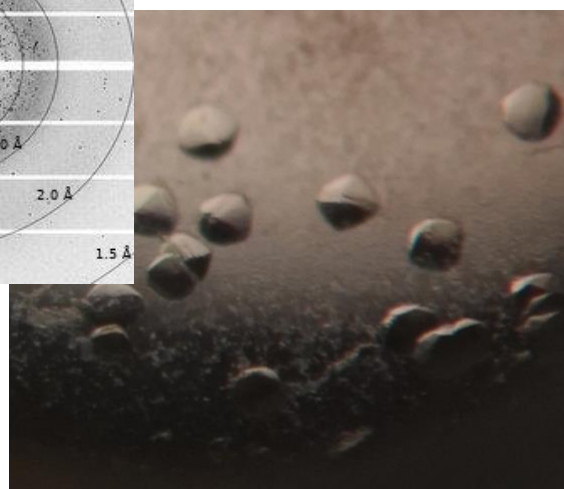
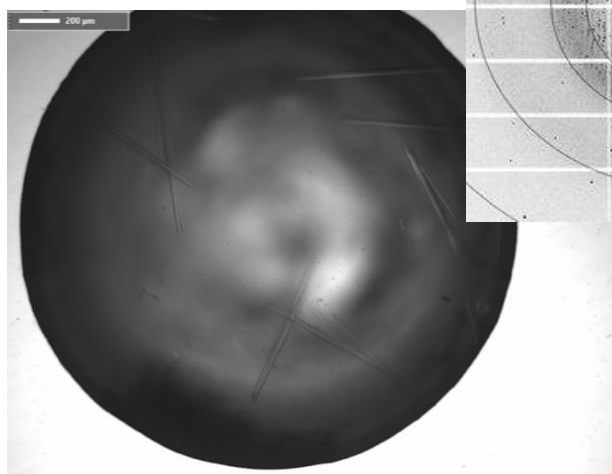
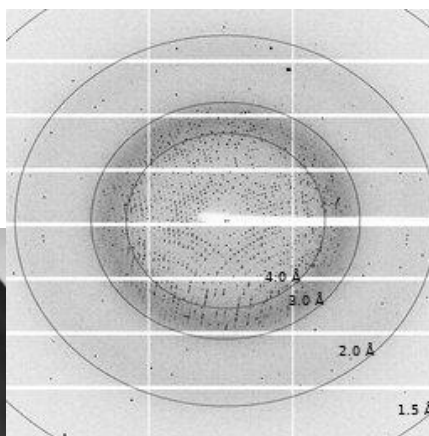
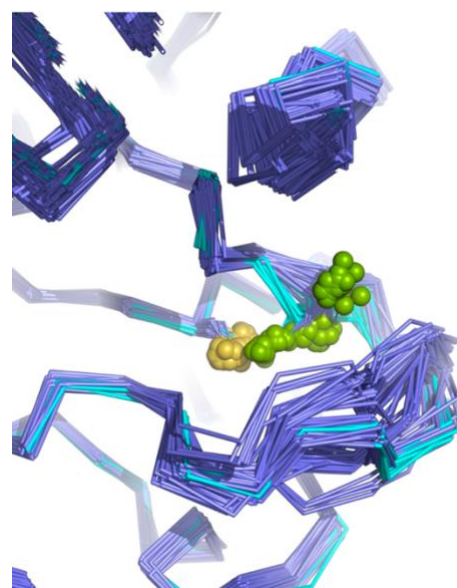
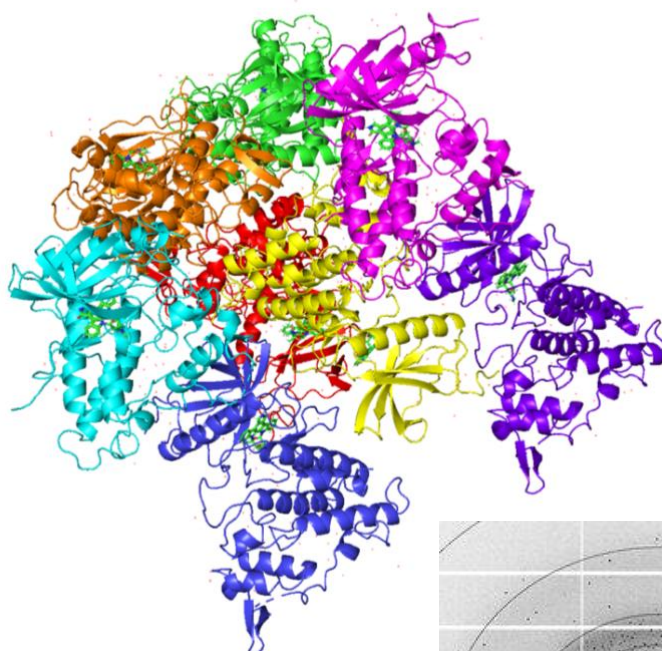
Faculty of Science and Technology

## The unique disulfide linked activation loop of DYRK kinases and possible redox activity control

*Studies on the kinase DYRK1A*

Maja Bele Dyrendalsli

Master's Thesis in Molecular Science KJE-3900 June 2022



## ABSTRACT

Most protein kinases are activated through phosphorylation of the activation loop (AL), which in turn stabilizes the active structure through salt bridge formation between the phosphate group and the guanidium group of the arginine residue of a highly conserved His-Arg-Phe (HRD) sequence. In DYRK kinases, the arginine of HRD is replaced by a cysteine (C286) which stabilizes the AL structure through disulfide bridge formation with a cysteine (C312) in the DFGSSC sequence. The AL has a known activating phosphorylation site at Y321, as is the case for most protein kinases. The conservation of the HCD sequence in DYRK kinases is a strong indication that it may function as a redox sensitive controller of DYRK activity. The purpose of this project is to investigate effects of the state of the disulfide bridge on enzyme catalytic and ligand binding properties. A DYRK1A mutant was designed to eliminate the disulfide bridge. It was expressed and purified following the same protocol as for the wt. The wt and the mutant were both crystallized with the kinase inhibitor Staurosporine, and the structures were solved by molecular replacement to a resolution of 2.33 Å and 2.59 Å, respectively. The structures were analyzed and compared with respect to experimental binding data and effects of disulfide bridge formation or elimination. Molecular dynamics (MD) simulations (SHROEDINGER) were performed with the intent to compare diverse disulfide bridge states. Ligand binding and enzyme catalytic properties were analyzed using a combination of techniques, including activity assays, microscale thermophoresis, and isothermal calorimetry.

## ACKNOWLEDGEMENTS

I would like to thank Professor Richard A. Engh for finding me a master project in the kinase research group. I am grateful for the opportunity to work on DYRK kinases, which I find to be a highly interesting area of research. I would also like to thank Dr. Ulli Rothweiler for his help in the lab and in solving the structure of the DYRK1A wt and DYRK1A C312A mutant. I could not have had better supervisors. Thank you to the other members of the kinase group: Robin Jeske, Nico Wistermayer and Magdalena Škrlová for their help and collaboration in the lab. Thank you to everyone else at Norstruct for their help with equipment, procedures, and simply finding my way around the lab. I would also like to thank my family for their continuous support and encouragement.

## ABBREVIATIONS

$\beta$ -ME	$\beta$ -mercaptoethanol
$\Delta \epsilon$	Extinction coefficient
A	Ampere
Amp	Ampicillin
ATP	Adenosine triphosphate
AU	Absorbance Unit
bp	base pair
CV	Column Volume
Da	Dalton
DMSO	Dimethyl sulfoxide
dNTP	Deoxyribonucleotide
DYRK	Dual-specificity tyrosine phosphorylation-regulated kinases
<i>E. coli</i>	<i>Escherichia coli</i>
EDTA	Ethylenediaminetetraacetic acid
FT	Flowthrough
HEPES	4-(2-hydroxyethyl)-1-piperazineethanesulfonic acid
IPTG	Isopropyl $\beta$ -D-1-thiogalactopyranoside
ITC	Isothermal Titration Calorimetry
$K_m$	Michaelis-Menten constant for enzyme-substrate complex
LB	Lysogeny Broth
MPa	Mega Pascal
MilliQ water	Deionized water
MOPS	3-(N-morpholino)propanesulfonic acid
MST	Microscale thermophoresis
min	Minutes
OD	Optical density
o/n	Overnight
PBS-T	Phosphate-buffered saline with Tween20
PCR	Polymerase chain reaction

PEG	Polyethylene glycol
rpm	Rounds per minute
SDS-PAGE	Sodium dodecyl sulfate – polyacrylamide gel electrophoresis
SEC	Size exclusion chromatography
TB	Terrific broth
TEV	Tobacco Etch Virus
V <sub>max</sub>	Maximum velocity of catalytic reaction
wt	wildtype

# CONTENTS

## 1. INTRODUCTION

- 1.1. Protein kinases
  - 1.1.1. Function
  - 1.1.2. Structure
- 1.2. DYRK family
  - 1.2.1. Function
  - 1.2.2. Structure
- 1.3. Kinase inhibition in modern drug discovery
  - 1.3.1. Selected inhibitors and inhibition approaches
    - 1.3.1.1. Staurosporine
    - 1.3.1.2. Luciferin
    - 1.3.1.3. Peptides
  - 1.3.2. Dyrk inhibitors
- 1.4. Redox environments in biology and disease
  - 1.4.1. Redox levels in the cell
  - 1.4.2. Redox phenomena in disease
  - 1.4.3. Hypotheses of redox sensing in DYRK kinases
- 1.5. Ligand binding kinetics and thermodynamics
  - 1.5.1.1 IC<sub>50</sub> vs K<sub>D</sub> description
  - 1.5.2 Experimental methods
    - 1.5.2.1 Cook assay
    - 1.5.2.2 Thermal shift assay
    - 1.5.2.3 Isothermal calorimetry (ITC)
    - 1.5.2.4 Microscale Thermophoresis (MST)
- 1.6 Molecular dynamics

## 2 MATERIALS AND METHODS

- 2.1 Buffers and solutions
- 2.2 Site-directed mutagenesis DYRK1A
- 2.3 Expression of DYRK1A wt and mutant
- 2.4 Cell disruption
- 2.5 Protein Purification
  - 2.5.1.1 Affinity chromatography
  - 2.5.1.2 TEV cleavage
  - 2.5.1.3 Size exclusion chromatography (SEC)
- 2.6 SDS-PAGE
- 2.7 Nanodrop
- 2.8 Plasmid miniprep
- 2.9 Thermofluor Assay
- 2.10 Cook Assay
- 2.11 ITC
- 2.12 MST
  - 2.12.1 Confirming the protein concentration with Bradford assay

- 2.12.2 Protein labelling
- 2.12.3 Binding assay
- 2.13 Crystallography of DYRK1A wt and mutant
  - 2.13.1 Crystallization methods
  - 2.13.2 Data collection, structure solution
- 2.14 Molecular Dynamics
- 2.15 Structure alignments

### **3 RESULTS**

- 3.1 Mutagenesis
- 3.2 Purification of DYRK1A wt and mutant
- 3.3 Thermofluor Assay
- 3.4 Cook Assay
- 3.5 ITC
- 3.6 MST
- 3.7 Crystallography
  - 3.7.1 Crystallization and data collection
    - 3.7.1.1 DYRK1A wt
    - 3.7.1.2 DYRK1A C312A
  - 3.7.2 Crystal structures
    - 3.7.2.1 DYRK1A wt in complex with STU
    - 3.7.2.2 DYRK1A C312A in complex with STU

### **4 DISCUSSION**

- 4.1 Superposition of DYRK1A structures
  - 4.1.1 Superposition of all DYRK1A structures
  - 4.1.2 Activation loop structural variability
  - 4.1.3 Superposition with the DYRK1A C312A mutant structures
- 4.2 Thermofluor: Effects of oxidant/reductant on melting temperature
- 4.3 Molecular Dynamics: Does MD hint at accessibility to conserved cysteine residues?

### **FUTURE WORK**

### **SUMMARY**

### **APPENDIX**

### **REFERENCES**

## **AIM OF STUDY**

The aim of this study is to investigate effects of the state of the disulfide bridge in DYRK1A on enzyme catalytic and ligand binding properties. The DYRK1A gene is located on the DSCR region on chromosome 21 and is known to play a role in several neurodegenerative diseases, such as Alzheimer and Parkinson. It is therefore of great interest to acquire information about inhibition of this kinase.

# 1 INTRODUCTION

## 1.1 Protein kinases

### 1.1.1 Function

Protein kinases are members of the kinase superfamily and are responsible for the regulation of a variety of cellular functions through catalyzing the phosphorylation of substrates. (1) (2) When ATP and a substrate bind to a protein kinase, the  $\gamma$ -phosphate from ATP is transferred to the substrate and the product and ADP are released from the catalytic site. This reaction requires magnesium to take place, as well as residues that facilitate the binding of the substrates and others that enhance the formation and release of the products. The catalytic domain of the protein kinases must undergo conformational changes to switch between active and inactive states. (3)

The human kinome contains 518 protein kinases, of which 478 contain a eukaryotic protein kinase (ePK) domain. (4) Human kinases are key players in metabolism, transcription, cell cycle progression, cytoskeletal re-arrangement, cell movement, apoptosis, and differentiation. Consequently, dysregulation of protein kinases plays a significant role in human disease. (4) (5)

Protein kinases are separated into three different subgroups: serine/threonine kinases (STKs), tyrosine kinases (TKs) and dual-specificity kinases, depending on their preferred phosphoacceptor residue. (6)

### 1.1.2 Structure

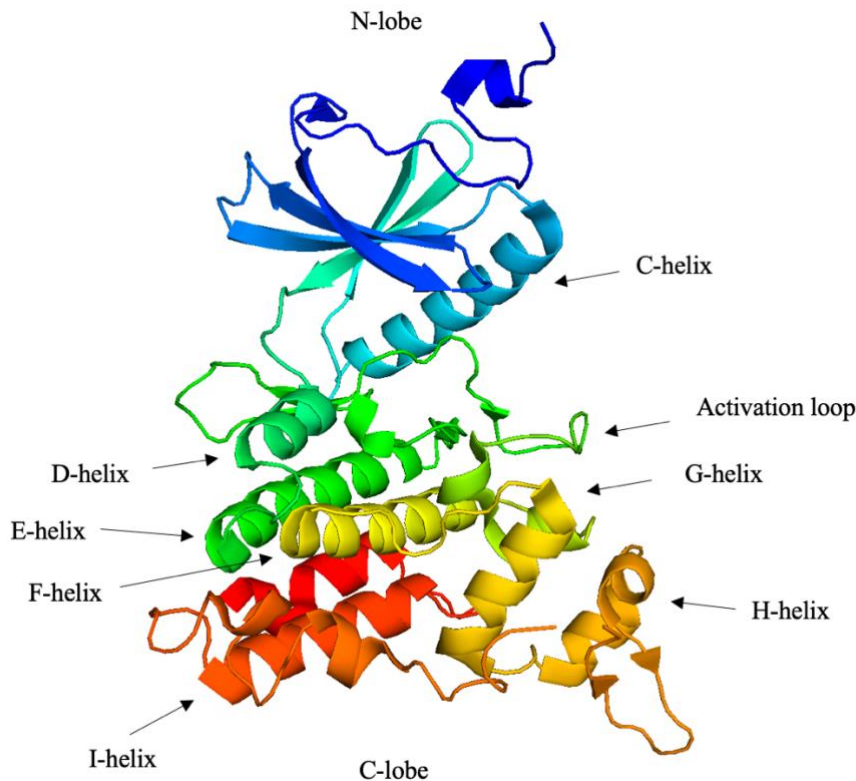


**Figure 1: An overview of the catalytic domain of protein kinases.** The illustration was made in Pymol(7), using a structure of DYRK1A (4NCT(8)).

The catalytic domain of protein kinases consists of approximately 250 residues and is made up of two subdomains: an N-terminal lobe (N-lobe) and a C-terminal lobe (C-lobe). The structure of the catalytic domain is illustrated in Figure 1. The C-lobe primarily consists of alpha-helices, while the N-lobe normally consists of one helix and five beta strands. The C-lobe is mainly responsible for substrate recognition, and for bringing the substrate adjacent to ATP for phosphorylation. (9) (10, 11) Structural studies on the catalytic domain have shown that the alpha C-helix is a key element in conformational regulation, due to its flexibility. (12)

The C-terminal domain is typically 20-30 amino acids in length and contains a conserved Asp-Phe-Gly (DFG) motif at the beginning of the A-loop. The conformation of the DFG-motif is essential for the catalytic activity of the kinase. In the catalytically active *DFG-in* state, two  $Mg^{2+}$  ions in close proximity to the DFG aspartate and the catalytic loop coordinate

the transfer of ATP phosphate groups. When the kinase is in its inactive *DFG-out* state, the side chains of Asp and Phe are flipped, resulting in the Asp turning in the opposite direction of the binding site. This hinders  $Mg^{2+}$ -coordination and consequently there is no catalytic activity in the *DFG-out* state. (13)

NMR studies on protein kinase A (PKA) and crystal structures of other protein kinases in various conformational states have shown that switching between the two states also entails significant conformational changes among key elements of the catalytic core. (14)

Other important catalytic motifs, in addition to DFG, include the ATP/ $Mg^{+}$  binding motif “VIAK”, the catalytic HRD motif, and the activation segment. (15) The activation segment (AS) in protein kinases runs from the “DFG” motif to the “APE” motif. It is anchored by the DFG at the N-terminus and the P + 1 loop at the C-terminus. (16) The conserved APE motif plays a part in stabilizing both the activation loop and the P+1 loop. (17) The activation segment is a flexible element, along with the regulatory spine (RS).

The R-spine consists of two residues from each lobe, RS1 to RS4, and is a distinctive feature of active kinases when assembled. (18) The residues, RS1, RS2, RS3 and RS4, come from the HRD motif, the DFG motif, the  $\alpha$ C-helix, and the  $\beta$ 4-strand, respectively, and are all crucial parts of the protein kinase. The catalytic spine, also known as the C-spine, is made up of a series of hydrophobic residues. It consists of two conserved residues from the N-lobe, and six from the C-lobe and is only completed after the adenine ring of ATP binds in the ATP binding pocket, leading the two lobes to close when the two parts of the spine come together. While assembly of the R-spine defines activation, assembly of the C-spine poises the kinase for catalysis. (19)

A range of regulatory mechanisms play a part in controlling the protein kinase switch, such as allosteric regulation, where the catalytic activity is modified by conformational changes that take place in the catalytic domain when a ligand or a regulatory protein binds. Because many human diseases are, at least partly, a result of abnormal regulation of protein kinase activity, it is essential for the development on new drugs and therapies that we understand how protein kinase activity is controlled by conformational changes. (14)

Between the two lobes is the glycine-rich loop, which sits above the adenosine triphosphate (ATP) adenine ring. These two are connected by a peptide strand, and together they form the active site of the protein kinases. (1) The glycine-rich loop (GxGxxG) is a highly conserved sequence motif in protein kinases. (19) It sits between  $\beta 1$  and  $\beta 2$  and covers the  $\beta$  and  $\gamma$ -phosphates of the ATP. It is a key player in both phosphoryl transfer and ATP/ADP exchange during the catalytic cycle. (1, 20)

## 1.2 DYRK family

### 1.2.1 Function

Dual-specificity tyrosine-regulated kinases (DYRKs) belong to the CMGC group of the eukaryotic kinome. (21) This group includes Cyclin-dependent kinases (CDKs), Mitogen-activated protein kinases (MAPKs), Glycogen synthase kinases (GSKs), and Cdc2-like kinases (CLKs). (22) DYRK is an evolutionary conserved family, consisting of five members: DYRK1A and DYRK1B (class 1 DYRKs) and DYRK2, 3, and 4 (class 2 DYRKs.) (23, 24) DYRK kinases distinguish themselves from other kinases in their ability to phosphorylate both aromatic (tyrosine) and aliphatic (serine, threonine) amino acid residues. (25)

DYRKs are activated through auto-phosphorylation of a conserved Y residue in the AL during protein translation. (26) DYRK kinases phosphorylate a wide range of substrates and play an important role in many cellular processes. They are believed to serve important biological functions both during development and maintaining homeostasis in adult life. Dysregulation of DYRK kinases is thus associated with a large range of pathologies. (23) DYRK1A is involved in several human nervous system diseases, including Alzheimer's disease, Down syndrome, autism, and Parkinson's disease. DYRKs have also been shown to play a part in diabetes, cancer, leukemia, and several infections. (24)

DYRK1A, which is the human orthologue of the *Drosophila* *mnb* (minibrain) gene, is mapped to human chromosome 21q22.2, which is in the Down syndrome critical region (DSCR) (27, 28) Down Syndrome (DS) is caused by partial or complete trisomy of chromosome 21, and it

is the most common chromosomal disorder associated with abnormal brain development. Trisomy of chromosome 21 also leads to early onset of Alzheimer-type pathology. (27)

## 1.2.2 Structure

The DYRK family of kinases exhibit little sequence similarity except for a small segment immediately preceding the catalytic domain, which is known as the Dyrk homology box (DH box) . (29) A multiple sequence alignment of the five members of the DYRK family is shown in Figure 2, where the conserved HCD motif and the DFGSSC sequence are highlighted by a red box.



**Figure 2: Multiple sequence alignment of the DYRK family.** A multiple sequence alignment was performed on the five members of the DYRK family, using sequences obtained from the UniProt database.(30) The following accession numbers were used: DYRK1A (Q13627), DYRK1B (Q9Y463), DYRK2 (Q92630), DYRK3 (O43781) and DYRK4 (Q9NR20). The alignment was performed on the residues corresponding to the kinase domain for each of the five protein kinases. The conserved HCD motif and the DFGSSC sequence are highlighted with red boxes. Jalview(31) and Mview(32) were used to align and view the sequences, respectively.

The catalytic domain of DYRK1A shares the conventional fold of protein kinases, with the ATP-binding pocket sitting in a cleft between the N-lobe and the C-lobe. The two lobes are connected by a hinge region where the mainchain atoms hydrogen-bond to ATP. (33)

### 1.3 Kinase inhibition in modern drug discovery

The first synthetic protein kinase inhibitors were described by Japanese researchers in 1984 and were based on an isoquinoline sulfonamide structure. This was followed by Fasudil, a Rho kinase inhibitor, becoming the first protein kinase inhibitor to be approved for medical use. It was crystal structures of isoquinoline compounds, and their protein kinase complexes that proved that the interactions of the inhibitors could successfully mimic ATP. Great advances have been made since 1984, and more than 70 kinase inhibitors are now approved for clinical use. (34) The first drug developed with the intent of targeting a specific protein kinase to treat a disease to be approved was Imatinib in 2001. (35) It is used in the treatment of chronic myeloid leukemia (CML), which is a hematological stem cell disorder. (35) (36) CML is characterized by a reciprocal translocation between chromosomes 9 and 22, resulting in what is known as the Philadelphia chromosome. (37) (36) Imatinib inhibits the Abelson (ABL) tyrosine kinase, which is expressed as a deregulated fusion protein of the abl cellular oncogene from chromosome 9 and the bcr gene of chromosome 22, termed BCR–ABL, (35) (37)

#### 1.3.1 Selected inhibitors and inhibition approaches

Most protein kinase inhibitors bind at the ATP binding site, which sits at the interface between the N-lobe and the C-lobe. (38) These are called ATP-competitive inhibitors and can further be classified as either type I inhibitors or type II inhibitors, depending on the position of a conserved DFG motif in the structurally flexible activation loop, which affects the functional state of the protein kinase. (39) (40) Inhibitors of type I target the ATP binding site of the kinase when the activation loop is phosphorylated, and the kinase is in its active conformation. (41) This is called the *DFG-in* state. (40) Type I inhibitors are often characterized by a heterocyclic ring system, which imitates the purine ring of the adenine moiety of ATP, occupying its binding site. (42) An example of a type I inhibitor is Erlotinib, an epidermal growth factor receptor tyrosine kinase inhibitor (EGFR TKI) which has proven efficacy in the treatment of advanced non-small cell lung cancer (NSCLC).(43)

A struggle of type I inhibitors is that the high conservation of the ATP binding pocket within the kinome has made it difficult for specific kinase inhibition to take place. (44) Type II inhibitors on the other hand bind to the kinase in its inactive conformation, commonly known as the *DFG-out* state, in which they occupy a hydrophobic pocket only present in this conformation. This gives them a higher selectivity than type I inhibitors, because the inactive conformation is less conserved. (40) an example of a type II inhibitor is Ponatinib, which is used in the treatment of chronic myeloid leukemia (CML) or Philadelphia chromosome-positive acute lymphoblastic leukemia (ALL).(45)

### 1.3.1.1 Staurosporine

Another example of a type I inhibitor is Staurosporine - a natural product and a high-affinity inhibitor of a large range of mammalian protein kinases. (46) It binds to the ATP binding site of the protein kinases and makes a number of contacts with both the hinge region and the two catalytic lobes. (47) The structure of Staurosporine is shown in Figure 3.

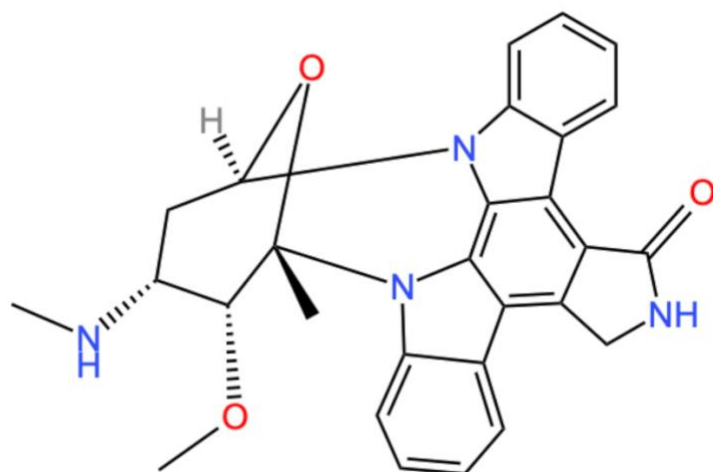


**Figure 3: Structure of the high-affinity protein kinase inhibitor Staurosporine.** The structure was drawn in ChemDraw.(48)

A systematic analysis involving 20 protein kinases revealed that most of them show a very high sensitivity to Staurosporine, with the majority having  $IC_{50}$  values in the low nanomolar range. (47) While Staurosporine itself is not used as a therapeutic agent, it has proven invaluable in the search of novel drugs in the field of cancer, based on kinase inhibitors. (49)

It is the precursor of Midostaurin (PKC412), also called *N*-benzoyl-staurosporine. (50)  
Midostaurin is a small-molecule kinase inhibitor that is approved by the US Food and Drug Administration for treatment of FLT3-mutant acute myeloid leukemia (AML). (51)

### 1.3.1.2 *D*-Luciferin

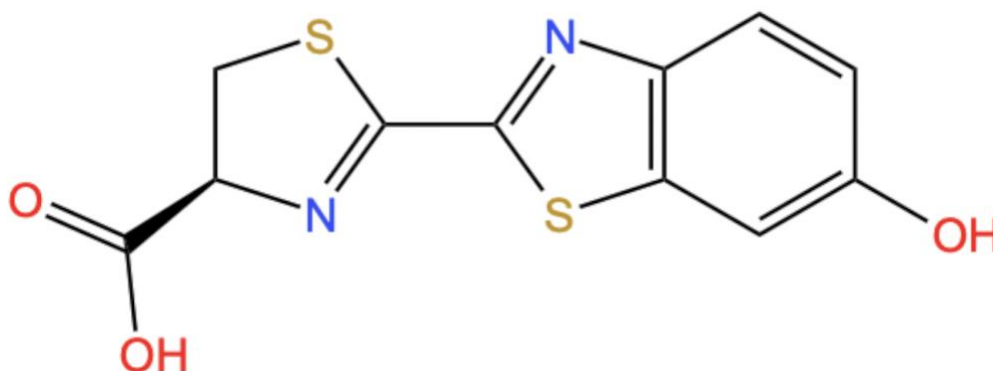


**Figure 4: The structure of D-Luciferin.** The structure was drawn in ChemDraw.(48)

D-luciferin is a substrate to the enzyme firefly luciferase and is commonly used in luciferase catalyzed bioluminescence assays for *in vitro* studies. (52, 53) The structure of D-Luciferin is shown in Figure 4. Inhibition profiling has shown that a small set of protein kinases are significantly inhibited by D-luciferin. This is particularly true for members of the CMGC group, including the DYRK-family. (53)

### 1.3.1.3 *Peptides*

It is not only within the field of ATP-competitive inhibitors that advancements are made. Protein kinase inhibitors that bind to the protein substrate-binding site are also popular targets for development. This would get around the issue of the high conservation of the ATP binding pocket and would greatly increase the possibility of developing successful kinase-specific inhibitor ligands. The idea gained momentum when a peptide inhibitor of PKA with high specificity and nanomolar affinity was identified. (54)

### 1.3.2 Dyrk inhibitors

Compounds originally designed to target other protein kinases have proved to also inhibit DYRK1A efficiently. This includes 2-dimethylamino-4,5,6,7-tetrabromo-1*H*-benzimidazole (DMAT) and 4,5,6,7-tetrabromo-1*H*-benzotriazole (TBB), which were both developed as CK2 inhibitors. Other examples include TG003, which was initially designed to target CLKs, and Purvalanol A, which was intended to target CDKs. The downside to all these inhibitors is that their low selectivity makes them less valuable for signaling pathway analysis. (55)

Profiling studies have also identified the two plant compounds, epigallocatechin (EGCG) and Harmine as inhibitors for DYRK1A. EGCG, which is one of the main polyphenolic constituents of tea, inhibits DYRK1A with an  $IC_{50}$  value of 0.33  $\mu$ M. (56) For Harmine, a  $\beta$ -carboline alkaloid,  $IC_{50}$  values of approximately 0.1  $\mu$ M have been reported. (57) Harmine has shown both anti-inflammatory and antitumor activities and has shown great potential in the treatment of diabetes. (58)

The involvement of DYRK1A has been identified in multiple pathways relevant to pancreatic  $\beta$ -cell proliferation, and studies have shown that inhibition of DYRK1A in pancreatic  $\beta$ -cells leads to enhanced proliferation and promotes glucose-stimulated insulin secretion (GSIS) without the risk of hypoglycemia. (59) (60) Restoring functional  $\beta$ -cell mass is a highly prioritized therapeutic goal for both type 1 and type 2 diabetes. (61)

## 1.4 Redox environments in biology and disease

### 1.4.1 Redox levels in the cell

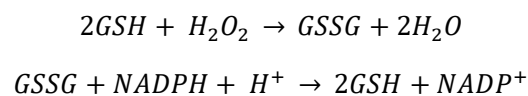
Redox signaling involves two types of reactions: oxidation reactions - in which a nucleophile (reducing agent) gives away electrons, and reduction reactions – in which an electrophile (oxidizing agent) receives electrons. In redox signaling, two-electron oxidations are more common than one-electron oxidations. (62) The redox environment in the cell is a result of the balance between the production of reactive oxygen species (ROS) and reactive nitrogen species (RNS), as well as their removal which is executed by antioxidant enzymes and small-

molecular-weight antioxidants. (63) ROS and RNS are collective terms describing oxygen-containing and nitrogen-containing chemically reactive molecules, respectively. (64)

The level of ROS is of great importance, due to the role they play in cell signaling, which in turn has a huge impact on numerous cellular pathways. This includes cell growth, survival, angiogenesis, and differentiation. (64)

Cysteine, along with histidine, methionine, tryptophan, and tyrosine, is one of the amino acids that is readily oxidized. If cysteine is ionized and exists as a thiolate, however, it is indisputably the most easily oxidized amino acid by ROOH. (62)

Glutathione is the most prevalent cellular thiol, often present at levels ranging from 0.1-10 mM. (65) It is made up from cysteine, glycine and glutamine, and is a natural reservoir of reducing power, which can be utilized to fight oxidative stress. (66) The sulfhydryl group (SH) of glutathione is the cause of its protective action against reactive oxygen species (ROS) and oxidative damage. Enzymes such as glutathione peroxidase and glutathione reductase are necessary to facilitate the action. Glutathione can either be in its reduced form (GSH), or in its oxidized form (GSSG). In animal tissue, glutathione peroxidase catalyzes the reduction of hydrogen peroxide and lipid peroxide in the presence of GSH, resulting in GSH being oxidized to GSSG. GSSG can be reduced to GSH by glutathione reductase when nicotinamide adenine dinucleotide phosphate (NAD(P)H) is present. (66) The reactions are shown in the following equation:



NADPH and its oxidized form, NADP<sup>+</sup>, plays a significant role in maintaining a balanced redox environment. (67) Another important pair, nicotinamide adenine dinucleotide (NAD<sup>+</sup>) and its reduced form, NADH, are pivotal for driving redox reactions in energy production. (68)

Reducing agents are often added to assays to prevent the cysteines from being oxidized in the target proteins. (69) Reducing agents such as dithiothreitol (DTT) and  $\beta$ -mercaptoethanol (BME) attack the disulfide bonds in proteins and cause them to shuffle.(70)

#### **1.4.2 Redox phenomena in disease**

Research has shown that cancer cells suffer from increased levels of ROS. (71) Higher levels of ROS is generated in cancer cells as a result of multiple processes, such as inactivation of tumor suppressor genes, activation of oncogenes and malfunction of the mitochondria, which creates a need for a more potent antioxidant system. The mitochondria is the primary endogenous source of ROS in mammalian cells as ROS is a by-product of oxidative phosphorylation (OXPHOS). (64)

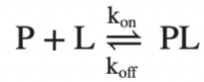
Other diseases in which dysregulated redox regulation plays a part include diabetes (72), aging (73) and a range of neurodegenerative disorders. (74). This includes Alzheimer's disease (75), Parkinson's disease (PD), Huntington's disease (HD), and amyotrophic lateral sclerosis (ALS.) (76)

#### **1.4.3 Hypotheses of redox sensing in DYRK kinases**

The conservation of the HCD sequence in DYRK kinases is a strong indicator that the cysteine may function as a redox sensitive controller of DYRK activity. Modification of cysteine residues is known to be a key regulatory process in cell signaling.(77) An example of this is the intramolecular disulfide bridge formed in kinases MKK6 and MAP2Ks, resulting in their inactivation through blocking ATP binding. (78)

## 1.5 Ligand binding kinetics and thermodynamics

Ligand binding kinetics describes the rate at which a protein and a ligand bind to one another. In a situation where the protein and ligand are mixed in a solution, their association can be written as,



Here P is the protein, L is the ligand, PL is the protein-ligand complex,  $k_{\text{on}}$  is the kinetic rate constant for the binding (forward) reaction, and  $k_{\text{off}}$  is the kinetic rate constant for the unbinding (reverse) reaction. The units of  $k_{\text{on}}$  and  $k_{\text{off}}$  are  $M^{-1}\cdot s^{-1}$  and  $s^{-1}$ , respectively.

At equilibrium, the forward and reverse reactions should balance each other, giving rise to the following equation:

$$k_{\text{on}}[P][L] = k_{\text{off}}[PL]$$

where the square brackets represent the equilibrium concentration of any molecular species.

The binding constant,  $K_b$ , is then calculated as follows:

$$K_B = \frac{k_{\text{on}}}{k_{\text{off}}} = \frac{[PL]}{[P][L]} = \frac{1}{K_d}$$

Where  $K_b$  has a unit of  $M^{-1}$ , and  $K_d$  is the dissociation constant. A high binding affinity is therefore obtained when you have a fast binding rate and a slow dissociation rate. (79)

It is important to gain insight into ligand-protein interactions to learn about the molecular-scale biological processes in living systems, and for screening drugs. A number of techniques have been developed, but it has proven challenging to quantify the binding kinetics of small molecules to proteins, due to the sensitivity of technologies decreasing with the size of the ligand. (80)

### 1.5.1 IC<sub>50</sub> vs K<sub>D</sub>

The half-maximal inhibitory concentration (IC<sub>50</sub>) is the most common way of measuring a drug's efficacy. The IC<sub>50</sub> value provides information about the concentration of a drug needed to inhibit a biological process by half. (81) (82) It is an important pharmacodynamic index of drug effectiveness.

In pharmacodynamics, the affinity of a drug to a target is commonly assessed by evaluating drug response curves. In such cases, a steeper curve would indicate tighter binding. The IC<sub>50</sub>, which is a critical index of the dose response curve, is used to compare the binding affinities of different drugs to the same target. While IC<sub>25</sub> and IC<sub>75</sub> can also be used, IC<sub>50</sub> is usually a superior index because the curve is normally steepest in the middle, which minimizes the estimation error for IC<sub>50</sub> as opposed to the alternatives. (82) IC<sub>50</sub> value can further be used to determine the equilibrium dissociation constant K<sub>d</sub> – another measure of binding affinity - using the Cheng-Prusoff equation: (83) (84)

$$IC_{50} = K_i \left( 1 + \frac{[S]}{K_d} \right)$$

Where [s] is the substrate concentration. The K<sub>d</sub> shows the concentration of free ligands at which half of the receptors are in a complex at binding equilibrium. (85) It is a fundamental parameter in terms of comparing the binding strength of different ligands and inhibitors to a binding partner. The K<sub>d</sub> is determined by plotting concentrations of bound versus free ligands as binding curves. (84)

In a system where one ligand (L) binds to one protein (P) and one type of protein-ligand complex is formed, the K<sub>d</sub> can be described by the following equation:

$$K_d = \frac{[P][L]}{[PL]}$$

Where the square brackets indicate the equilibrium concentrations. (86)

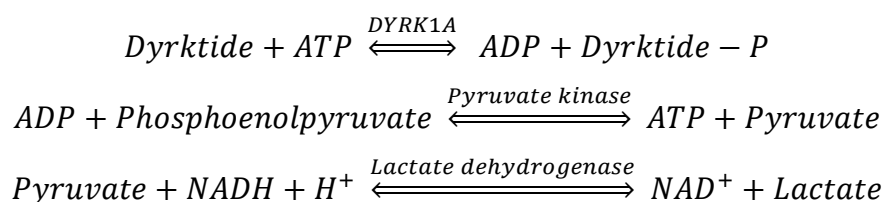
$K_d$  is often seen to be more precise than  $IC_{50}$ . This is due to  $IC_{50}$  not directly measuring a binding equilibrium, meaning that the values are highly dependent on variables such as measurement conditions and mechanism of inhibition. It is, however, very convenient for the characterization of in vivo activity of a drug for which it is difficult to access the factors contributing to its potency.(87)

The ability to measure drug affinity is paramount for drug discovery and acquiring information about signal transduction, cell division and other fundamental biological processes. (88) (86)

## 1.5.2 Experimental methods

### 1.5.2.1 Cook assay

The Cook assay was originally published for PKA, (89) and was later adapted for DYRK1A. (99) It is a kinase activity assay that measures the NADH consumption while keeping the ATP concentration constant. The rate of disappearance of NADH is monitored spectroscopically at 340 nm. The following reactions take place in the assay:



In the first reaction we have peptide phosphorylation and ADP release via coupled enzymatic reactions. In the second reaction, pyruvate kinase restores ATP levels by dephosphorylating phosphoenolpyruvate (PEP), which creates pyruvate. Lastly, lactate dehydrogenase creates lactate and  $\text{NAD}^+$  from pyruvate, NADH and  $\text{H}^+$  in its reverse reaction.

### 1.5.2.2 Thermal shift assay

Thermal shift assay is a biophysical screening technique used for detection of protein-ligand interactions. The thermal stability of a protein is compared to that of the protein in the presence of a ligand. A shift in melting temperature indicates binding. When a protein folds, the hydrophilic residues will be on the surface, exposed to the solvent, while the hydrophobic residues will make up the interior. This is to minimize the free energy. An increase in temperature leads to a destabilization of the protein structure, resulting in denaturation and an exposure of the hydrophobic core. The process is monitored with a real-time PCR instrument and fluorescence detection. (90) A typical melting curve is illustrated in Figure 5.

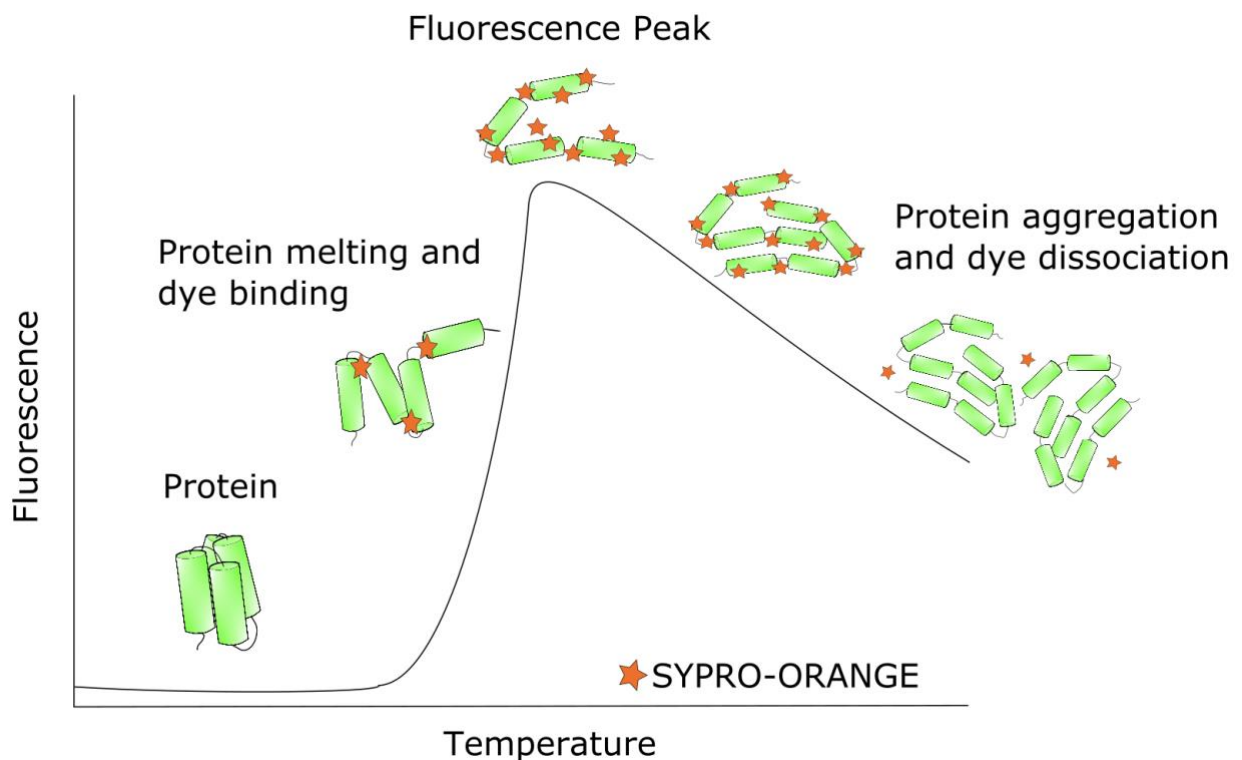


**Figure 5: Melting curve of a protein during the ThermoFluor assay.** The dye binds to the protein after it unfolds, leading to an increase in the measured Fluorescence. The figure was made using Inkscape.(91)

The SYPRO Orange fluorescence emission is monitored while the temperature is systematically increased, allowing for an observation of the thermal denaturation of the protein in many conditions simultaneously. The thermal shift can be used to identify optimal buffer conditions, as well as identifying small molecule ligands, which commonly stabilize

the protein upon binding. It is a popular technique because it is quick and requires small amounts of protein. (92)

The source of the fluorescence signal can either stem from innate tryptophan fluorescence or, more commonly, a dye that gives a stronger fluorescence signal when it binds to the hydrophobic residues in the unfolding protein. ANS (1-anilinonaphthalene-8-sulfonic acid), or its derivative bis-ANS, and SYPRO Orange are examples of such dyes. (93)

### ***1.5.2.3 Isothermal Titration Calorimetry (ITC)***

ITC is a technique widely used to obtain enzymatic kinetic information. (94) In a typical ITC experiment, addition of a binding partner (titrant) into another binding partner (titrate) is performed over time, through one or more individual injections. Heat is then measured as a change in temperature or in the power necessary to maintain the same temperature for both the reference cell and the sample cell. This energy can then be converted into a binding enthalpy, using the volume of the cell and the concentration of the reactants-(95)

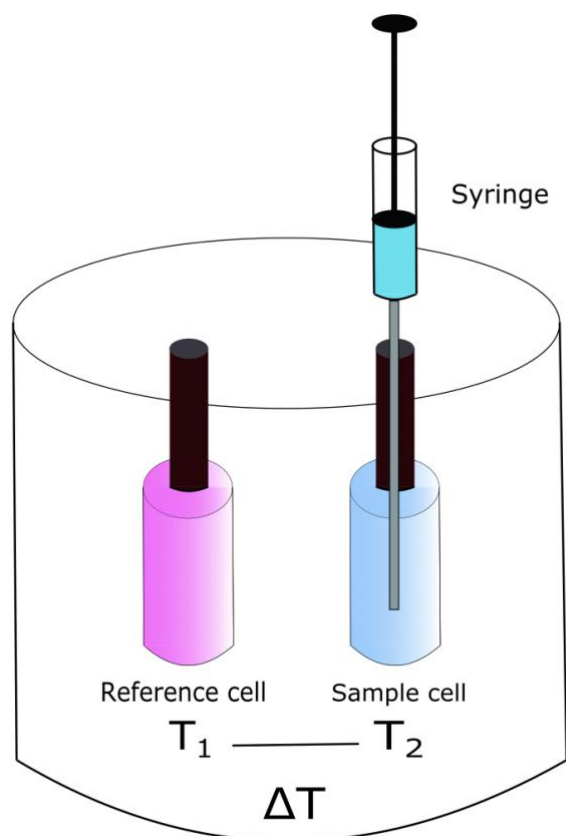


**Figure 6: Equipment for performing ITC measurements.** The machine is built up of two cells – a reference cell and a sample cell. The difference in temperature between the two cells after injection of the sample and addition of a titrant, is then used to calculate binding enthalpies. The figure was made using Inkscape.(91)

ITC is currently the only technique with which one can determine the binding affinity and the binding enthalpy in a single experiment. (96)

Advantages of using ITC as a technique for enzyme measurements include that the approach is entirely general since most chemical reactions either produce or consume heat, and as a result the method can be applied to all enzymes. The measurements can be performed under dilute, physiological solution conditions. There is also no delay between the mixing of the solutions and the start of the experiment, as is the case in many spectroscopic measurements. In addition, ITC detects heat flow in real time and provides a direct readout of the enzyme activity and the way in which it is affected by the inhibitors, as opposed to deducing them from substrate and product concentrations, as is often the case with other techniques. (97)

#### 1.5.2.4 *Microscale Thermophoresis*

Microscale Thermophoresis (MST) is a technique that allows for measuring binding affinities of binder-ligand systems, as a function of the molecules directional movement in a temperature gradient. (98) The method is used extensively because it requires small amounts of sample and it's easy to use. (99)

An infrared laser is used to create a local temperature gradient with optical heating. The 2-6°C temperature increase will spark the diffusion of molecules – a phenomenon known as thermophoresis. If a ligand binds to the target molecule, this leads to a change in the molecule's size, charge, or solvation, which in turn alters the diffusion rate, which is translated into a change in the local concentration of the molecules. The fluorescence of the labeled molecules is monitored in response to thermophoresis and translated to a binding curve from which  $K_d$  can be evaluated. (100)

In most MST experiments in which the goal is to quantify an interaction, the concentration of the labeled molecule is kept constant, whereas the concentration of the unlabeled binding partner is varied. It is common to start at a concentration that is a minimum of 10 times larger than the expected dissociation constant. From there one proceeds down to sub-stoichiometric concentration with respect to the labeled molecule. The changing fluorescence signal depending on the concentration of target is given by the following equation:

$$F_{norm} = (1 - x)F_{norm}(unbound) + xF_{norm}(bound)$$

Where  $F_{norm}(unbound)$  is the normalized fluorescence,  $F_{norm}(bound)$  is the normalized fluorescence of complexes, and  $x$  is the fraction of labeled molecules bound to their targets. (101)

## 1.6 Molecular dynamics

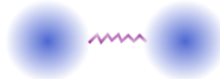
MD simulations have in recent years become a widely used technique for studying the structure and dynamics of macromolecules. Simulations often include as many as ~50,000–100,000 atoms. The systems are initially prepared from nuclear magnetic resonance (NMR) or crystallographic data, or- in cases with no available experimental data- the systems are built through homology-modelling. Once a simulation system is built, force-fields can be used to obtain the forces acting on each atom present in the simulation. (102)

In MD, the motion of the atoms is simulated by solving Newton's equation of motion simultaneously for all atoms in the system: (103)

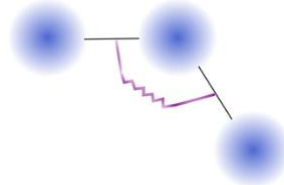
$$F = (mv) \frac{d}{dt} = ma$$

The chemical, geometric and mechanical properties of molecules consist of “bonded” (bonds, bond angles, torsional angles) and “nonbonded” (van der Waals, Coulombic) potential energy terms, which make up the so-called force field and give the total potential energy for the system. (104) A graphical representation of the components of a force field is shown in Figure 7.

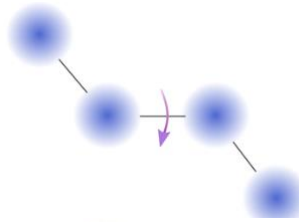
$$U(R) = \sum_{Bonds} k_r (r - r_{eq})^2$$



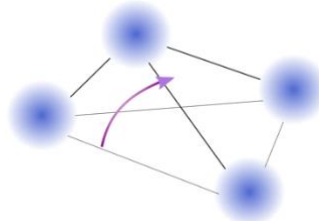
$$+ \sum_{Angles} k_\theta (\theta - \theta_{eq})^2$$



$$+ \sum_{Dihedrals} k_\phi (1 + \cos[n\phi - \gamma])$$



$$+ \sum_{Improper} k_\omega (\omega - \omega_{eq})^2$$



$$+ \sum_{i < j}^{Atoms} \epsilon_{ij} \left[ \left( \frac{r_m}{r_{ij}} \right)^{12} - 2 \left( \frac{r_m}{r_{ij}} \right)^6 \right]$$



$$+ \sum_{i < j}^{Atoms} \frac{q_i q_j}{4\pi\epsilon_0 r_{ij}}$$

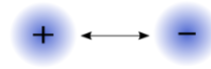


**Figure 7: Graphical representation of the components of a force field.** A force field is made up of bonds, angles, torsions, van der Waal's interactions and Coulombic interactions. The blue spheres in the illustration represent atoms. (105) The figure was made using Inkscape.(91)

## 2 MATERIALS & METHODS

### 2.1 Buffers & Solutions

All buffers and solutions used in this project are listed along with their contents in Table 1.

**Table 1: Buffers and solutions used in this project**

<b>Buffer/Solution</b>	<b>Contents</b>	<b>pH</b>
Buffer A	500 mM NaCl, 50 mM PO <sub>4</sub>	8.0
Buffer B	50 mM PO <sub>4</sub> 3-, 300 mM NaCl, 500mM imidazole	8.0
Buffer C (TEV)	50 mM Tris, 200 mM NaCl, 2 mM b-mercaptoethanol	7.5
Buffer D (GF)	50 mM mops, 50 mM KCl	6.8
LB agar	1% (w/v) Tryptone, 0.5% (w/v) Yeast extract, 1% (w/v) NaCl, 1.5% (w/v) Agar-agar in MilliQ water	
LB media	1% (w/v) Tryptone, 0.5% Yeast Extract, 1% (w/v) NaCl in MilliQ water	
PBS-T	50 mM Tris-HCl pH 7.4, 150 mM NaCl, 10 mM MgCl <sub>2</sub> in MilliQ water	
TB	1.2% (w/v) Tryptone, 2.4% (w/v) Yeast extract, 0.5% Glycerol in MilliQ water	

### 2.2 Site-directed mutagenesis DYRK1A

The QuickChange II site-directed mutagenesis protocol(106) was employed to produce the DYRK1A C312A mutant. The strategy for the mutagenesis is illustrated in four steps in Figure 8.

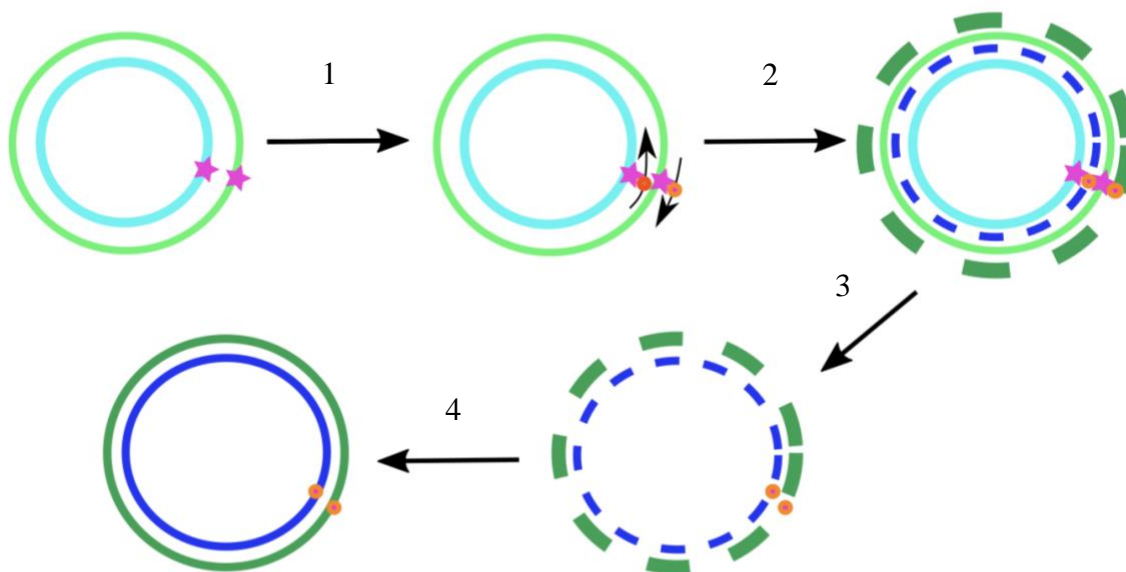


**Figure 8: Illustration of the QuickChange II site-directed mutagenesis.** The figure is modified from the QuickChange™ II site-directed mutagenesis protocol (Agilent Technologies.) The pink star represents the spot where the point mutation should take place in the plasmid, which is represented by the circles. The orange spheres are the primers that were designed to possess the desired mutation (C312A). In step 1, the plasmid is denatured, and the primers then anneal to the correct spot on the plasmid. In step 2, the Pfu Turbo™ DNA polymerase replicates the parental plasmid and incorporates the primers containing the desired mutation. In step 3, Dpn1 digests the parental plasmid which does not contain the mutation. In the fourth and final step, plasmid is transformed into competent cells and the nicked plasmids are ligated and amplified.

A primer was first designed using the QuickChange Primer Design Program.(107) The nucleotide sequence of the forward and reverse primers is listed in Table 2. The mutated nucleotides are highlighted yellow.

**Table 2: Primers designed for site-directed mutagenesis**

Point mutation	Fwd/Rvs.	Nucleotide sequence
C312A	Fwd	CTCTGCCCCAACTGAGCAGAACTGCCAAAGTCAACTATC
	Rvs	GATAGTTGACTTTGGCAGTTCTGCTCAGTTGGGGCAGAG

The FASTA-formatted DNA sequence for DYRK1A was uploaded and the nucleotides corresponding to the mutation C312A were specified. The primer was ordered and stored in the freezer at -20°C until it was used. The primer was then dissolved in H<sub>2</sub>O to a concentration of 100 ng/μl.

Four sample reaction mixtures were prepared using the recipe provided by the QuickChange II site-directed mutagenesis kit, as described in Table 3. 5, 10, 20 and 50 ng dsDNA template was used. The primer concentration was kept constant. The PfuUltra HF DNA polymerase was added last. The reactions were cycled according to the parameters in Table 4.

**Table 3: Sample reaction.**

---

5 μl of 10x reaction buffer
X μl (5-50 ng) of dsDNA template
X μl (125 ng) of oligonucleotide primer #1
X μl (125 ng) of oligonucleotide primer #2
1 μl of dNTP mix
ddH <sub>2</sub> O to a final volume of 50 μl
1 μl <i>PfuUltra</i> HF DNA polymerase (2.5U/μl)

---

**Table 4: Thermal cycling parameters as proposed by the QuickChange protocol.(106)**

---

Segment	Cycles	Temperature	Time
1	1	95°C	30 seconds
2	12 for point mutations	95°C	30 seconds
	16 for single amino acid	55°C	1 minute
	changes	68°C	1 minute/kb of
	18 for multiple amino acid deletions or insertions		plasmid length

---

Following the temperature cycling, the reactions were placed on ice for two minutes to cool the reaction to  $< 37^{\circ}\text{C}$ .

1  $\mu\text{l}$  of the restriction enzyme (10 U/ $\mu\text{l}$ ) was added to each of the amplification reactions. They were gently and thoroughly mixed by pipetting up and down multiple times. The reaction mixtures were spun down in a microcentrifuge for 1 minute, followed by immediate incubation at  $37^{\circ}\text{C}$  for 1 hour to digest the parental (nonmutated) supercoiled dsDNA.

XL1-Blue supercompetent cells(108) were thawed on ice. 50  $\mu\text{l}$  of the cells were transferred to a prechilled 14 ml BD Falcon polypropylene round-bottom tube. 1  $\mu\text{l}$  of the Dpn 1-treated DNA from each sample reaction was transferred to separate aliquots of the supercompetent cells. The transformation reactions were gently swirled for mixing before they were incubated on ice for 30 minutes. The reactions were heat pulsed for 45 seconds at  $42^{\circ}\text{C}$  and were then placed on ice for 2 minutes. 0.5 ml of NZY+ broth was preheated to  $42^{\circ}\text{C}$  and added to the reactions. They were incubated at  $37^{\circ}\text{C}$  for 1 hour with shaking at 225-250 rpm.

250  $\mu\text{l}$  of each transformation reaction was plated on pre-made LB-ampicillin agar plates (2 plates per reaction). The transformation plates were incubated at  $37^{\circ}\text{C}$  for approximately 16 hours. Two colonies were picked and inoculated in 4 ml of LB-media with 4  $\mu\text{l}$  ampicillin and incubated at  $37^{\circ}\text{C}$  overnight with shaking at 220 rpm.

2 ml of the mini culture was used to isolate and purify the plasmid by QIAprep spin Miniprep kit. The plasmid was then sequenced.

### **2.3 Expression of DYRK1A wt and mutant**

1  $\mu\text{l}$  DNA and 50  $\mu\text{l}$  bacterial cells (BL21 Star Rare) were transferred into an Eppendorf tube and mixed by gently tapping on the walls of the tube. It was put on ice for 15 minutes, followed by heat shock for 45 minutes in a  $42^{\circ}\text{C}$  water bath. Back on ice again, 500  $\mu\text{l}$  LB and 50  $\mu\text{l}$  glucose was added to the Eppendorf tube. It was then incubated at  $37^{\circ}\text{C}$  for one hour.

After incubation, the solution was transferred to an Erlenmeyer flask containing 50 mL LB. 50  $\mu$ L ampicillin was added, and the solution was incubated at 37°C overnight.

The next day, the solution was transferred to a flask containing 900 ml TB and 100 ml salts. 1 ml ampicillin was added to the flask. This was followed by incubation at 37°C until the optical density reached 1.0. The temperature was then lowered to 17.8°C, and 1 mmol IPTG was added.

On the third day, the solution was poured into a centrifugation flask, and was centrifuged at 5000 rpm for 20 minutes. The pellet was stored in the freezer at -20°C.

## **2.4 Cell disruption**

The pellet was taken out from the freezer and was dissolved in 50 ml of Buffer A. 250  $\mu$ l Tween20 was added to the solution, which was then poured into a 100 ml beaker. The beaker was placed in an ice/water bath, and the protein solution was sonicated for 15 minutes, 4 seconds on and 8 seconds off. The maximum amplitude was set to 40% and the maximum temperature was set to 12°C.

After sonication, the solution was poured into two centrifuge tubes. The rotor JA-25.50 was used to centrifuge them for 60 minutes at 20 000 rpm, with a temperature of 4°C. The supernatant was then transferred to two 50 ml falcon tubes, approximately 25 ml in each.

## **2.5 Protein purification**

### **2.5.1 Affinity chromatography**

Äkta prime plus Fast Protein Liquid Chromatography (FPLC) system was employed to perform affinity chromatography on the protein.

A 5 ml HisTrap column packed with Ni Sepharose HP beads was washed with 15 ml of Buffer B, followed by 15 ml of Buffer A, before the protein solution was loaded onto the column with a peristaltic pump. A system wash was performed on the Äkta prime with Buffers A and B. The column was connected, and the program was started. The initial settings were 0% B, with a flow rate of 1 ml/min and a fraction size of 6 ml. The concentration of Buffer B was later set to 5%. A gradient with a length of 40 ml and a target of 100% B was started after the first peak in the chromatogram. The fraction size was changed to 2 ml. The run was ended once the target of 100% B was reached.

### **2.5.2 TEV cleavage**

TEV-protease cleavage was employed to remove the His-tags from the protein. The fractions corresponding to the peaks in the chromatogram were analyzed on an SDS-PAGE gel. The ones containing protein were then pooled. 1 ml TEV protease was added, and the protein solution was then transferred into a membrane using a syringe and a needle. The membrane was dropped into a 1L beaker containing Buffer C. The beaker was stored in the cold-room at 4°C o/n on stirring for the TEV cleavage to be performed.

The next morning, the sample was retrieved from the membrane using a syringe and a needle. Extra loops were connected to the Äkta prime to ensure that the volume of the loops surpassed the volume of the sample. A 1 ml HisTrap column was washed with Buffer A with a flow rate of 10 ml/min. The column was then disconnected, and the loops were washed with a flow rate of 30 ml/min, also with Buffer A. The protein sample was loaded into a syringe with a needle and was then injected onto the machine. The program was run with a flowrate of 1 ml/min and 0% B. The fraction size was set to 6 ml. After 25 ml had passed through (the size of the loop), the percentage of Buffer B was set to 5%. The gradient was started after the peak. An SDS-page was run, and the desired fractions were pooled and stored in a 50 mL falcon tube overnight.

### **2.5.3 Size exclusion chromatography**

A 120 mL HiLoad™ column was employed to perform size exclusion chromatography on the protein. A system wash was performed on the Äkta prime, with A as Buffer D and B as MilliQ water. The loop was washed by injecting water with a syringe. The SEC column was connected. A manual run was performed with water at 1 mL/min for 30 minutes. Another manual run was then performed with Buffer D for 120 minutes (1 CV = 120 ml). The protein was concentrated to a volume of less than 10 ml and was then injected onto the column using a syringe. The program was set to a flow rate of 1 ml/min, a fraction size of 2 ml and a pressure limit of 0.5. The fractions corresponding to the peaks were analyzed on an SDS-Page gel, and the ones containing protein were pooled. The gel filtration column was washed with water overnight. The protein was concentrated to 10 mg/ml and was divided into eppendorfs with 100 µl in each, before it was frozen in the -82°C freezer.

## **2.6 SDS-PAGE**

Sodium Dodecyl Sulphate-Polyacrylamide Gel Electrophoresis (SDS-PAGE) was used to analyze the protein samples, and to verify the purity after each step in the purification routine. Depending on the number of fractions to be analyzed, 10-, 12- and 15-well BIO-RAD gels were used. A molecular weight marker was always pipetted into the first well for comparison. For the remaining wells, 30 µl of the protein samples were mixed with 10 µl of a sample buffer in Eppendorf tubes. The tubes were then placed in a heat block at 95°C for approximately 5 minutes to denature the protein. Each of the samples was then loaded into its own well on the gel. The SDS-PAGE was run at 200 V, 90 mA for 35 minutes. Afterwards, the gel was rinsed with MilliQ water before it was stained with SimplyBlue Safestain and boiled in the microwave for approximately 30 seconds. It was then placed on an orbital shaker. It was later rinsed with MilliQ water and placed back on the shaker.

## **2.7 Nanodrop**

The concentrations of protein and DNA were measured using the Nanodrop 2000c (Thermo Science) spectrophotometer(109). 200 nl MilliQ water or buffer was loaded as a blank, before 200 nl of the protein sample was loaded and used for measuring the concentration.

## **2.8 Plasmid miniprep**

The QIAprep spin Miniprep Kit was used for isolating the plasmid. 2 ml of the sample was transferred to two microcentrifuge tubes and was then centrifuged at 8000 rpm for 3 minutes. The supernatant was removed and 250  $\mu$ l of Buffer P1 was added to each of the tubes. The pellets were resuspended using a pipette. 250  $\mu$ l Buffer P2 was added, and the solutions were mixed by inverting the tubes six times. 350  $\mu$ l Buffer N3 was added, and the solutions were mixed in the same manner as before. The tubes were centrifuged for 10 minutes at 13 000 rpm. The supernatant was transferred to a QIAprep spin column by pipetting. It was centrifuged for 60 seconds, and the flow-through was discarded. 0.75 ml Buffer PE was added, and the tubes were centrifuged for 60 seconds. The flow-through was discarded, and another 60 seconds of centrifugation was performed. The QIAprep spin column was placed in a 1.5 ml microcentrifuge tube. To elute DNA, Buffer EB was added to the center of the QIAprep spin column. It rested for 1 minute and was then centrifuged for 1 minute. The concentration was measured with Nanodrop, and the plasmids were frozen at -20°C.

## **2.9 Thermofluor Assay**

A 5000x stock solution of Sypro Orange (S.O.) was diluted in water to create a 90x stock solution. 12.5  $\mu$ l buffer was pipetted into a 48-well white PCR-plate. 7.5  $\mu$ l of the 90x S.O stock was pipetted into each of the wells. The protein was diluted in buffer to a concentration of 10  $\mu$ M. The inhibitors were diluted to a concentration of 100  $\mu$ M. 5  $\mu$ l of the protein stock was added, followed by 1.25  $\mu$ L of the inhibitors. Finally,  $\beta$ -mercaptoethanol, peroxide and glutathione were added. The plate was sealed with optical-quality sealing tape. The program was run from 20-95°C.

## 2.10 Cook Assay

6 ml reaction premix was prepared according to the recipe in Table 5. The protein was diluted 1:40 in MOPS, with a final concentration of 5.95  $\mu\text{M}$ . 75  $\mu\text{l}$  of the reaction premix and 10  $\mu\text{l}$  protein was pipetted into a well, thoroughly mixed and analyzed. 75  $\mu\text{l}$  of the premix, 10  $\mu\text{l}$  of the protein and 10  $\mu\text{l}$  of ATP was then pipetted into the next well and were mixed and analyzed to measure the activity of the protein. A Molecular Device SpectraMax M2 plate reader was used for measuring the absorbance.

**Table 5: Reaction premix.** Recipe for 1 ml reaction premix.

---

0.5 ml MOPS (200 mM, pH 6.8)
0.1 M KCl (1 M)
10 $\mu\text{l}$ MgCl <sub>2</sub> (1 M)
10 $\mu\text{l}$ PEP (100 mM in H <sub>2</sub> O)
5 $\mu\text{l}$ DYRKtide (20 mM in H <sub>2</sub> O)
1 $\mu\text{l}$ 2-mercaptoethanol (1 M in H <sub>2</sub> O)
15 $\mu\text{l}$ Pyruvatkinase lactate dehydrogenase
20 $\mu\text{l}$ NADH (10.7 mM in H <sub>2</sub> O)
89 $\mu\text{l}$ H <sub>2</sub> O

---

10 mM Staurosporine was diluted in MOPS to three initial concentrations, 1 mM, 0.1 mM and 0.01 mM. 75  $\mu\text{l}$  of the premix, 10  $\mu\text{l}$  of the protein, 5  $\mu\text{l}$  of the inhibitor and 10  $\mu\text{l}$  of ATP was pipetted, mixed, and analyzed for each of the three dilutions. A new set of dilutions were made to cover the whole area from 0% inhibition to 100% inhibition.

## 2.11 Isothermal Calorimetry (ITC)

ITC measurements were performed the DYRK1A C312A mutant with D-Luciferin as a ligand. DYRK1A C312A was diluted in Buffer D to a concentration of 20  $\mu\text{M}$ . Luciferin was

diluted in Buffer D to a concentration of 200  $\mu\text{M}$ .  $\beta$ -mercaptoethanol was added to both the protein and the inhibitor to a final concentration of 1 mM. Buffer D was pipetted into the reference cell, while the diluted protein with BME was pipetted into the sample cell. The program was run at 20°C.

## **2.12 Microscale Thermophoresis (MST)**

MST measurements were performed on the DYRK1A C312A mutant with a peptide called “Rain”, obtained from the research project of PhD student Robin Jeske. DYRK1A wt has shown binding to the same peptide in previous MST experiments performed by Jeske.

### **2.12.1 Confirming the protein concentration with Bradford assay**

The Bradford assay was used to verify the concentrations of purified DYRK1A and DYRK1A C312A. Dye reagent was prepared by diluting one part Dye Reagent Concentrate with four parts DDI water. The solution was filtered to remove particulates. Seven dilutions of a BSA protein standard were prepared, with the following concentrations: 0.0 mg/ml, 0.05 mg/ml, 0.1 mg/ml, 0.2 mg/ml, 0.3 mg/ml, 0.4 mg/ml and 0.5 mg/ml. 10  $\mu\text{l}$  of each standard and sample solution was pipetted into separate wells on the 96-well microplate. Everything was assayed in triplicates. 200  $\mu\text{l}$  of the diluted dye reagent was pipetted into each of the wells. The solution was mixed by repeatedly pipetting up and down. The plate was incubated at room temperature for 5-10 minutes. Absorbance was measured at 595 nm, the optimal wavelength for the Coomassie dye-protein complex. A standard curve was constructed and was used to verify the concentration of the protein.

### **2.12.2 Protein Labeling**

A 100 nM dye solution was prepared by mixing 2  $\mu\text{l}$  of the dye (5  $\mu\text{M}$ ) and 98  $\mu\text{l}$  PBS-T buffer. The protein was diluted to a concentration of 200 nM. 100  $\mu\text{l}$  of the protein was then added to the Eppendorf tube containing the dye solution. The solution was incubated for 30

minutes at room temperature, before it was centrifuged for 10 minutes at 4°C and 15 000 g. The supernatant was transferred to a fresh tube.

### 2.12.3 Binding assay

25 µl of the ligand, “Rain”, was prepared in PBS-T buffer for a final concentration of 1000 nM. 10 µl of PBS-T was then added into 16 PCR- tubes, before 20 µl of the ligand was added into each of the tubes. 10 µl of the ligand was then transferred from the first PCR- tube into the second PCR- tube using a pipette. The two components were mixed thoroughly by pipetting up and down multiple times. 10 µl was then transferred from the second tube to the third tube and the same procedure was repeated for the remaining tubes. The extra 10 µl from tube number 16 was discarded. Next, 10 µl of the labeled protein was pipetted into each well and thorough mixing was performed. Finally, the capillaries were loaded, and the samples were measured using the Monolith NT.115 pico.

16 runs were performed, with ligand concentrations ranging from 1000 nM to 0.03 nM. The parameters for the experiment are shown underneath in Table 6.

**Table 6: Parameters used for the MST runs.**

Experiment type	Expert mode
Capillary count	16
Excitation color	Pico – RED
Excitation power	25%
MST power	High
Phase 1 duration	3
Phase 2 duration	20
Phase 3 duration	1
Evaluation strategy	On time 1.5 s
Cold region	-1.0 s – 0.0 s
Hot region	0.5 s – 1.5 s

## **2.13 Crystallography of DYRK1A wt and mutant**

### **2.13.1 Crystallization methods**

The crystallization trials for DYRK1A wt with STU and DYRK1A C312A with STU were performed using the vapor diffusion method. 100  $\mu$ L of the concentrated protein kinase (10 mg/ml) was mixed with 4  $\mu$ L of STU (10 mM) in DMSO. The final concentration of STU in the trials was 400  $\mu$ M. The commercial screens SG1<sup>TM</sup> (Molecular Dimensions) and JCSG-plus<sup>TM</sup> (Molecular Dimensions) were used for the initial trials to find crystallizing conditions. The Formulatrix robot was used to pipette solutions from the deep well into 96-well sitting drop crystal plates. The ratio between the protein solution and the reservoirs were 1:1, with the drops consisting of 200 nl of each. The crystallization trials were performed at room temperature. The conditions that yield crystals were further optimized on a 24-well screen with a grid design. The Formulatrix robot was used for dispensing the reservoir solutions, with a volume of 500  $\mu$ l in each well. The hanging drop method was used for the 24-well plates, with a 2+2  $\mu$ l ratio of protein solution to reservoir solution.

The crystals were fished from the wells and frozen in liquid nitrogen, with LV oil as a cryoprotectant. They were then sent for X-ray data collection.

### **2.13.2 Data collection and structure solution**

The crystal structures of the DYRK1A wt in complex with STU, and the DYRK1A C312A mutant in complex with STU was solved by Dr. Ulli Rothweiler by molecular replacement with MolRep of the CCP4 software package.(110) The structure was further refined using Refmac(111) and Phenix.(112)

## **2.14 Molecular dynamics**

Maestro (SCHROEDINGER)(112) was used for performing molecular dynamics simulations on the structure of DYRK1A in complex with PKC-412.

The pdb file of 4NCT (DYRK1A with PKC-412) was downloaded and opened in Maestro. The structure was split by chain and chain B was deleted, leaving only chain A. The protein was prepared for the dynamic simulation using the Protein Preparation Wizard and Energy Minimization. The bond between the sulfur on C286 and the one on C312 was removed to model an open disulfide bridge. Desmond implementation of MD from the Schrodinger Molecular Modelling package was used to perform the simulation. Default conditions were used and the total time for the trajectories when combined was 2 microseconds. The force field used for the MD simulations was OPLS4. (113)

To investigate the effects of the disulfide bridge, a range of measurements were performed using tools in Maestro. This includes analyzing the solvent accessible surface area (SASA) of C286 and C312 and measuring the distances between residues that are of particular interest, such as between the gatekeeper residue and STU.

## **2.15 Structure alignments**

76 DYRK1A crystal structures (Appendix) were identified in the Protein Data Bank (PDB) via a sequence search using the human DYRK1A sequence of the catalytic domain were loaded into Pymol, split into single catalytic domain objects using the “split\_chain” function, and superimposed with the “align” function.

### 3 RESULTS

#### 3.1 Mutagenesis

Site-directed mutagenesis was performed using the QuickChange II Site-Directed mutagenesis kit (Agilent technologies) with a plasmid of the DYRK1A wt as a template.

The sequencing results confirmed that the point mutation was successful. Nucleotides T and G were mutated to G and C, respectively, resulting in amino acid 312 changing from a Cysteine to an Alanine. The sequencing results are shown underneath in Figure 9. The upper row is the original chromatogram of DYRK1A wt, while the lower row is the chromatogram for the DYRK1A C312A mutant. The mutated nucleotides are highlighted by a yellow box.

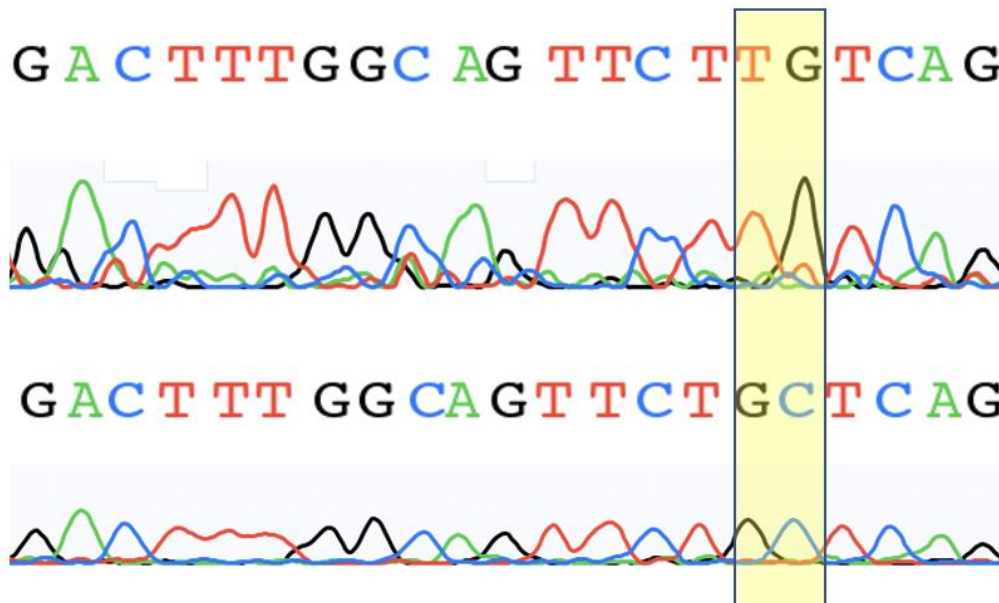
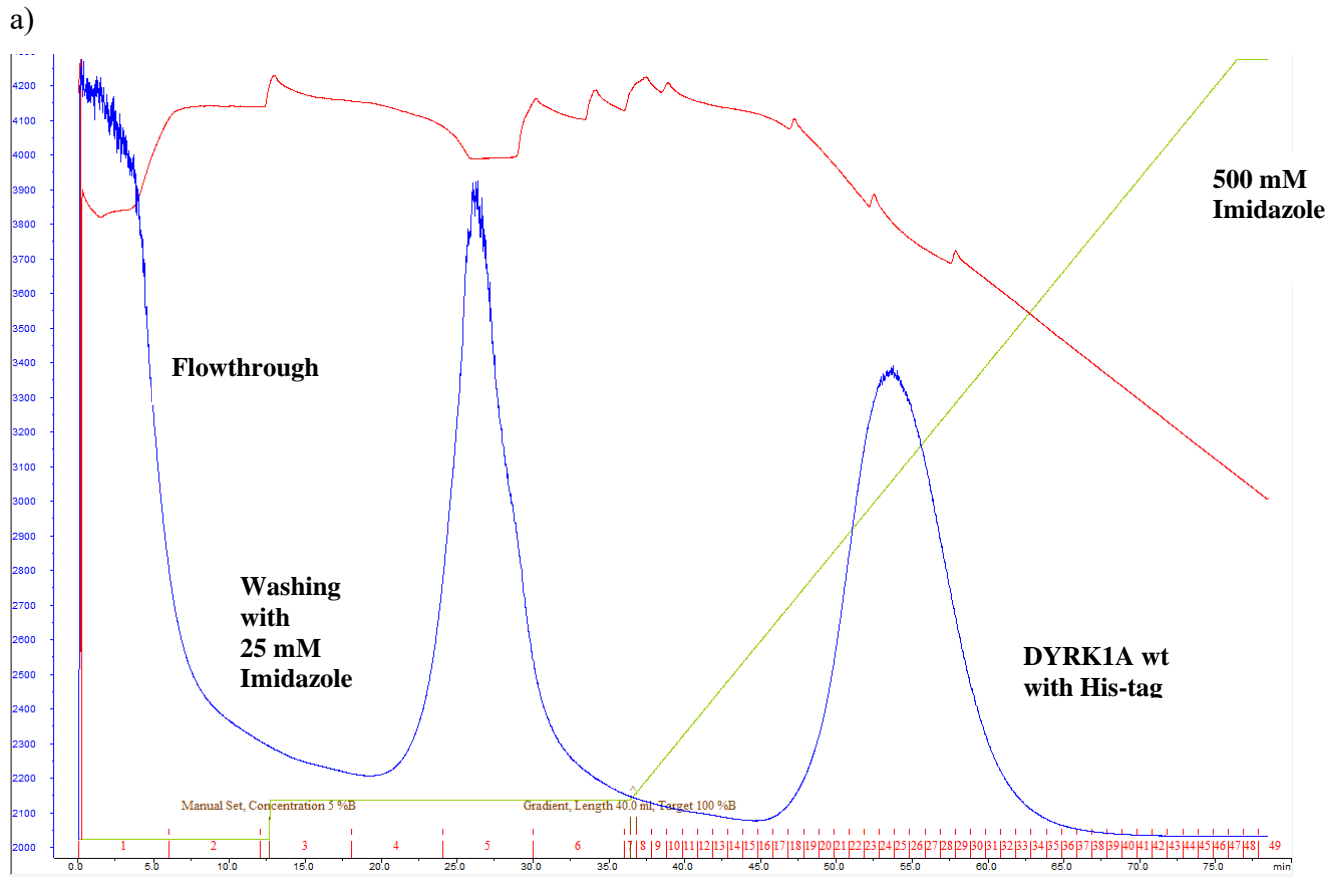


**Figure 9. Sequencing results for DYRK1A wt and DYRK1A C312A.** The sequencing chromatogram of DYRK1A wt is represented in the upper row, while the sequencing chromatogram of DYRK1A C312A is represented in the lower row. The mutated nucleotides are highlighted with a yellow box.

### 3.2 Purification of DYRK1A wt and mutant

DYRK1A wt and the mutant DYRK1A C312A were both successfully expressed. The same protocol was followed, and no noticeable difference was observed between the wt and the mutant during purification. The results included in the thesis are from purification of DYRK1A wt.

During the first step of the purification, DYRK1A wt was eluted on a 5 ml HisTag column with a flow rate of 1 ml/min and a pressure limit of 0.5 mPa. The elution buffer, Buffer B, contained Imidazole at a concentration of 500 mM. DYRK1A wt was eluted on a gradient starting at 5% Buffer B, which corresponds to 25 mM Imidazole, to 100% Buffer B. The percentage of Buffer B is represented as a green line in the chromatogram in Figure 10 a). The red line is the conductivity, and the blue line is the absorbance at 280 nm. The third peak in the chromatogram shows that DYRK1A wt eluted at approximately 40-50% of Buffer B (200-250 mM Imidazole). Fractions 1, 5, 17, 18, 20, 22, 24, 26, 28, 30 and 32 were analyzed on an SDS-PAGE gel. A photo of the gel is shown in Figure 10 b). It shows that fractions 20-32 contained DYRK1A wt.



b)

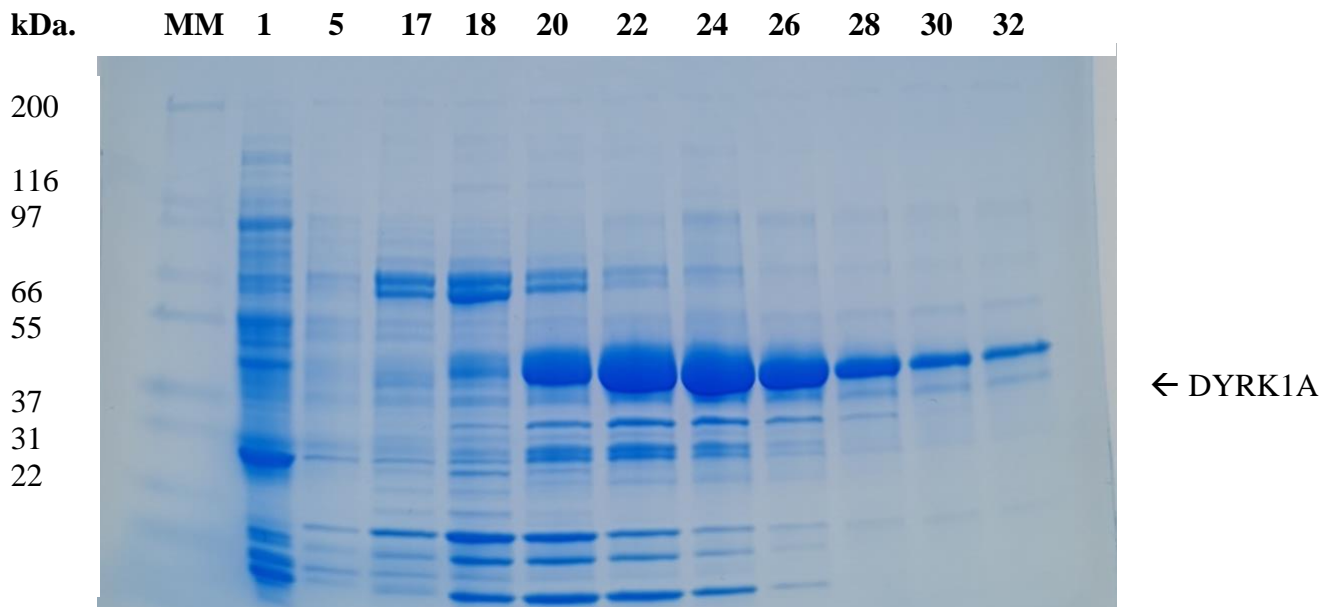
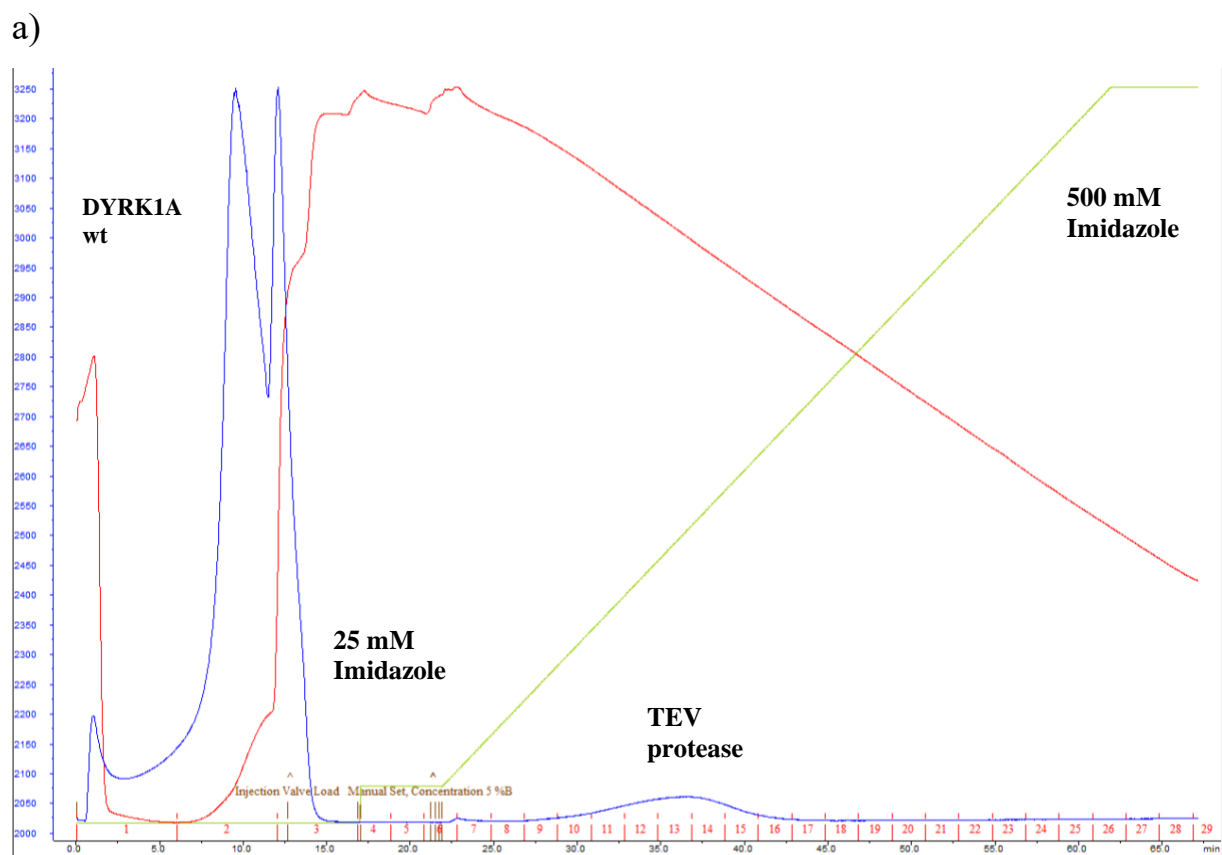


**Figure 10: Purification of His-tagged DYRK1A wt.** a) Chromatogram showing the affinity purification of His-tagged DYRK1A wt using a 5 ml HisTrap column. The red line is the conductivity, the green line is the percentage of the elution buffer (imidazole), and the blue line is the absorbance at 280 nm. b) SDS-PAGE gel of His-tagged DYRK1A wt after affinity purification. The molecular weight of DYRK1A is approximately 42 kDa. The band is clearly visible between the marker bands at 37 and 55 kDa.

These fractions containing DYRK1A wt were pooled and the his-tags were cleaved off by a TEV-protease overnight, before the second affinity chromatography was performed using the 1 ml HisTrap column. This time DYRK1A wt eluted before the start of the elution buffer gradient, confirming that the His-tags had been successfully cleaved off. The chromatogram is shown underneath in Figure 11 a). The small peak in absorbance in the middle of the gradient is the TEV protease and the cleaved His-tags. Fractions 1, 2, 3, 4, 5, 6, 7, 10 and 11 for analyzed on an SDS-PAGE gel, of which a photo is shown in Figure 11 b). Fractions 1-5 were pooled and further purified.



b)

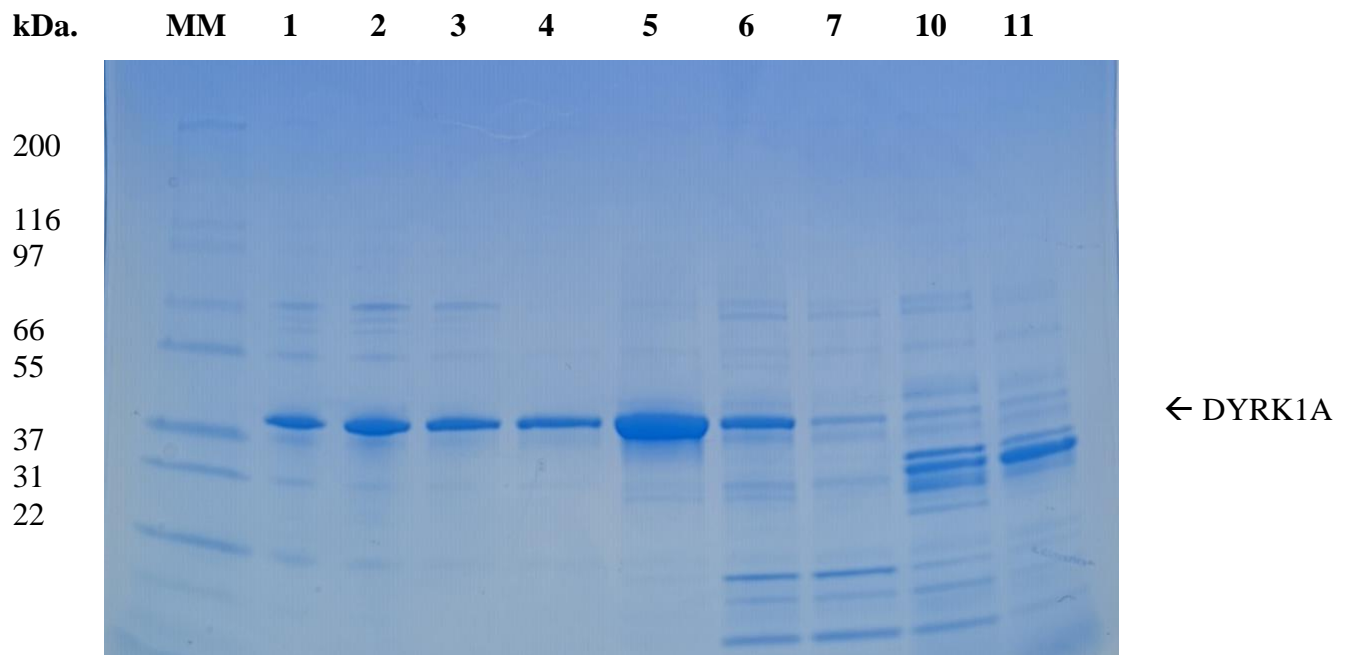


**Figure 11: Purification of cleaved DYRK1A wt.** a) Chromatogram showing the affinity purification of cleaved DYRK1A wt using a 1 mL HisTrap column. The red line is the conductivity, the green line is the percentage of the elution buffer (imidazole), and the blue line is the absorbance at 280 nm. b) SDS-PAGE gel of His-tagged DYRK1A wt after affinity purification. The band corresponding to DYRK1A wt is clearly visible between the marker bands at 37 and 55 kDa.

The last step of the purification was gel filtration (size exclusion chromatography), for which a 120 mL HiLoad™ column was employed. The sample was eluted at a flow rate of 1 ml/min for 1 CV. The chromatogram for the SEC is shown underneath in Figure 12 a). The large peak at approximately 80 ml is the elution of DYRK1A wt. Fractions 29, 30, 31, 33, 35, 37, 39, 42, 43, 44, 45, 46, 47 and 49 were analyzed on an SDS-PAGE gel, which is shown in Figure 12 b). Fractions 35-45 were pooled and concentrated to approximately 10 mg/ml. 1 L culture yield about 7 mg purified protein.

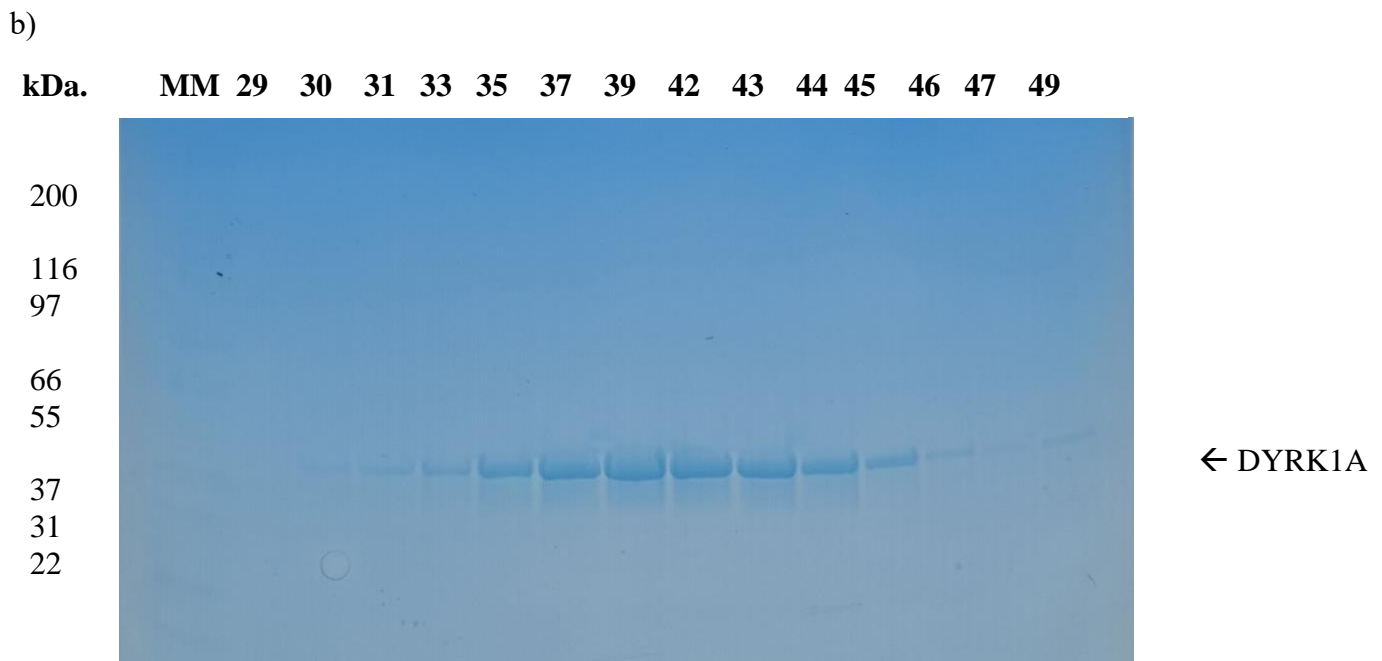
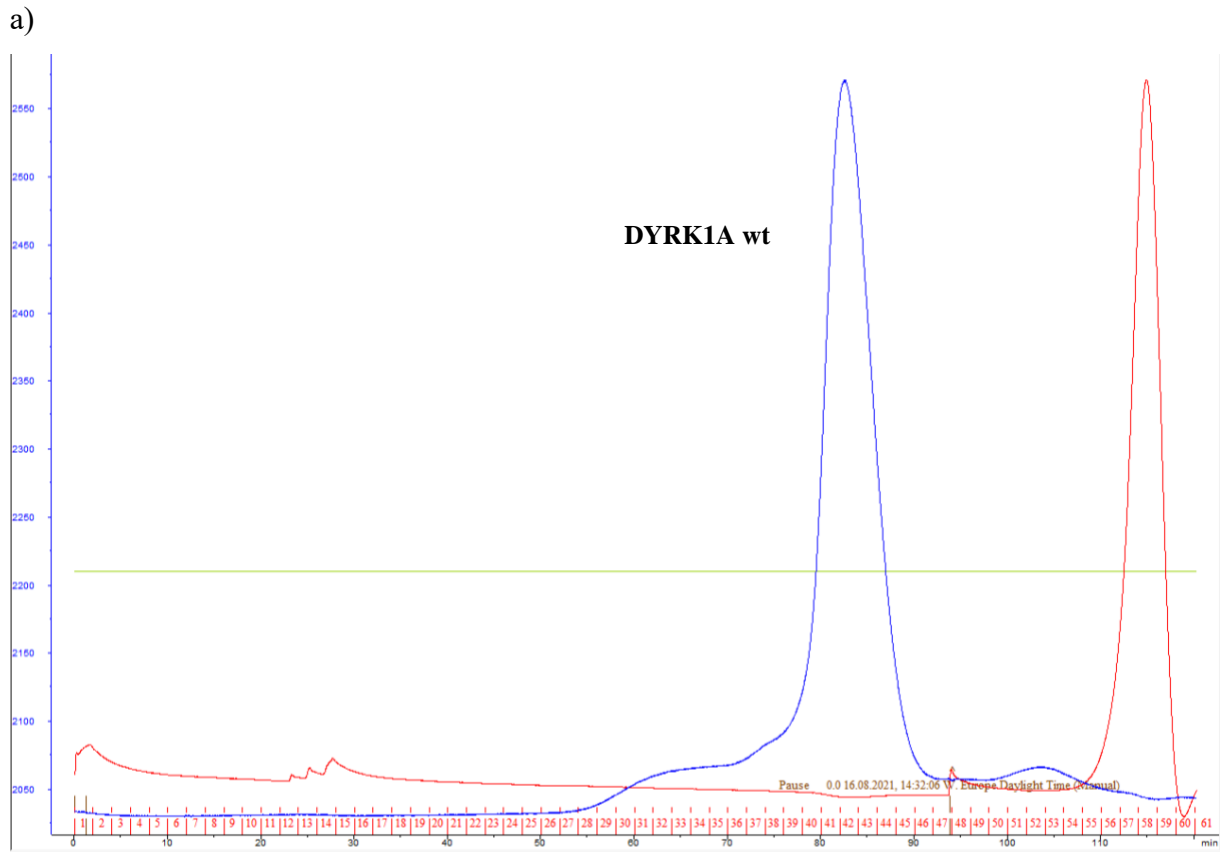


**Figure 12: Purification of DYRK1A wt.** a) Chromatogram showing the gel filtration (size-exclusion chromatography) of DYRK1A wt using a 120 mL column. The red line is the conductivity, the green line is the percentage of the elution buffer (imidazole), and the blue line is the absorbance at 280 nm. b) SDS-PAGE gel of DYRK1A wt after purification by SEC. The band corresponding to DYRK1A wt is clearly visible between the marker bands at 37 and 55 kDa.

### 3.3 Thermofluor assay

Multiple rounds of the assay were performed both with apo protein and with inhibitors present, to find the optimized conditions for carrying out the experiment.

The melting temperatures,  $T_m$ , for both DYRK1A wt and DYRK1A C312A are presented in Table 7 underneath. The redox condition for each experiment is given in the first column. *Untreated* means that no oxidant or reductant was added to the assay.  $\Delta T_m$  is the difference in melting temperature between the apo protein and the protein when bound to the inhibitor. Some of the data was uninterpretable, which is represented by  $x$  in the table.

**Table 7: Thermofluor measurements of DYRK1A wt and DYRK1A C312A with and without STU, AZ-191 and LUC as ligands.** Measurements were done with DYRK1A wt and DYRK1A C312A without ligands present, with STU, with AZ-191 and with LUC. All combinations were measured with untreated protein, with BME, with glutathione and with peroxide.  $T_m$  is the melting temperature of the protein, SD is the standard deviation,  $\Delta T_m$  is the difference in melting temperature when the protein is bound to a ligand as opposed to not being bound. Uninterpretable data is represented by x.

		DYRK1A wt		DYRK1A C312A	
		$T_m \pm SD$ (°C)	$\Delta T_m$ (Xligand-Xprotein)	$T_m \pm SD$ (°C)	$\Delta T_m$ (Xligand-Xprotein)
Untreated	Apo protein	42.90 ± 0.42		40.50 ± 0.14	
	Protein + STU	56.53 ± 0.12	13.63	54.00 ± 0.20	13.50
	Protein + AZ-191	59.47 ± 0.76	16.57	56.73 ± 0.23	16.23
	Protein + LUC	42.90 ± 0.14	0.00	40.60 ± 0.20	0.10
$\beta$ -ME (0.5 mM)	Apo protein	49.60 ± 0.87		35.00	
	Protein + STU	57.20 ± 0.92	7.60	53.00 ± 0.20	18.00
	Protein + AZ-191	57.73 ± 0.58	8.13	51.87 ± 6.64	16.87
	Protein + LUC	49.00	-0.60	35.00	0.00
$\beta$ -ME (560 mM)	Apo protein	44.20 ± 0.53		43.60 ± 2.26	
	Protein + STU	47.87 ± 1.75	3.67	45.53 ± 0.64	1.93
	Protein + AZ-191	49.60 ± 0.20	5.40	46.73 ± 0.12	3.13
	Protein + LUC	44.87 ± 0.51	0.67	44.40 ± 0.20	0.80
Glutathione (0.5 mM)	Apo protein	x		x	
	Protein + STU	57.47 ± 1.17	x	52.00	x
	Protein + AZ-191	57.60 ± 0.72	x	53.40 ± 0.35	x
	Protein + LUC	45.60	x	35.00	x
Peroxide (0.1 mM)	Apo protein	x		x	
	Protein + STU	50	x	54.07 ± 0.12	x
	Protein + AZ-191	50	x	53.00 ± 0.87	x
	Protein + LUC	43	x	36.47 ± 0.76	x

It is apparent from the results in Table 7 that DYRK1A wt has a consistently higher melting temperature than DYRK1A C312A. This is true for every condition except when Peroxide

(0.1 mM) is present in the assay. It can also be deduced from Table 7 that STU and AZ-191 both lead to an increase in melting temperature, while LUC seemingly has no effect. The highest melting point for the protein kinase is achieved when it is bound to AZ-191, with no reductant or oxidant present.

### 3.4 Cook assay

The  $V_{\max}$  values measured in the Cook assay were converted into kinase activity (%), which was plotted against the log concentrations of the inhibitor STU. The dose response curves were used to calculate the  $IC_{50}$  values, which tells us the concentration of a drug needed to inhibit a biological process by half. The dose response curve for DYRK1A wt and DYRK1A C312A are shown underneath in Figure 13 a and b, respectively.

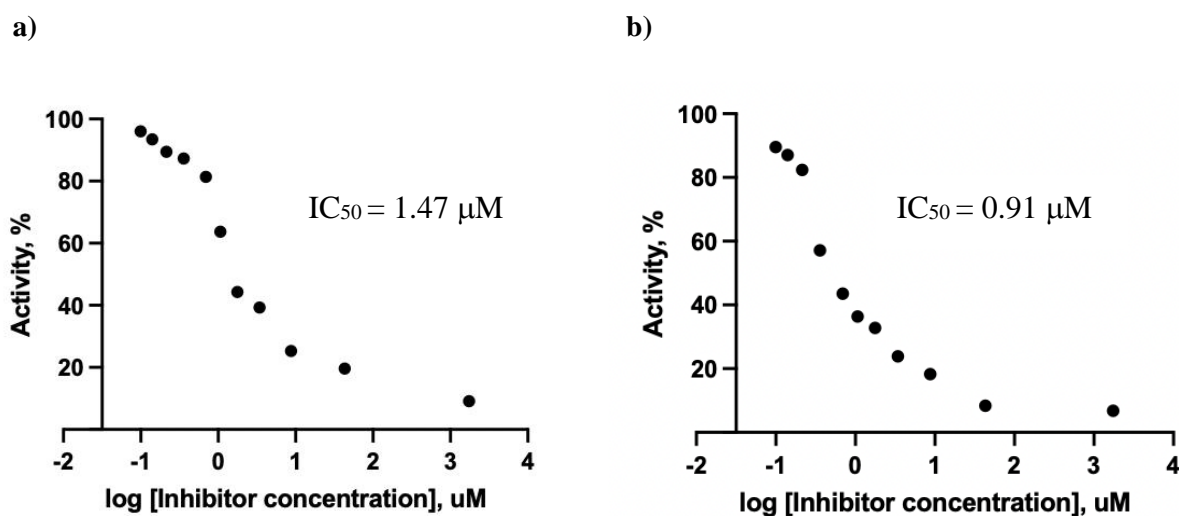


**Figure 13: Dose response curves for DYRK1A wt and DYRK1A C312A with STU.** a) Dose response curve for DYRK1A wt, plotted using data from the Cook assay. The x-axis represents the log concentration of the inhibitor ( $\mu\text{M}$ ) and the y-axis represents the activity of the protein kinase (%). The half-maximal inhibitory concentration ( $IC_{50}$ ) value was calculated to be 1.47  $\mu\text{M}$  b) Dose response curve for DYRK1A C312A. The  $IC_{50}$  was calculated to be 0.91  $\mu\text{M}$  for the mutant. The graphs were made using Graphpad Prism.(114)

The IC<sub>50</sub> value for DYRK1A wt was calculated to be 1.47 μM, while the IC<sub>50</sub> value for the DYRK1A C312A mutant was calculated to be 0.91 μM. These results would indicate that the wt is more resistant to Staurosporine inhibition than

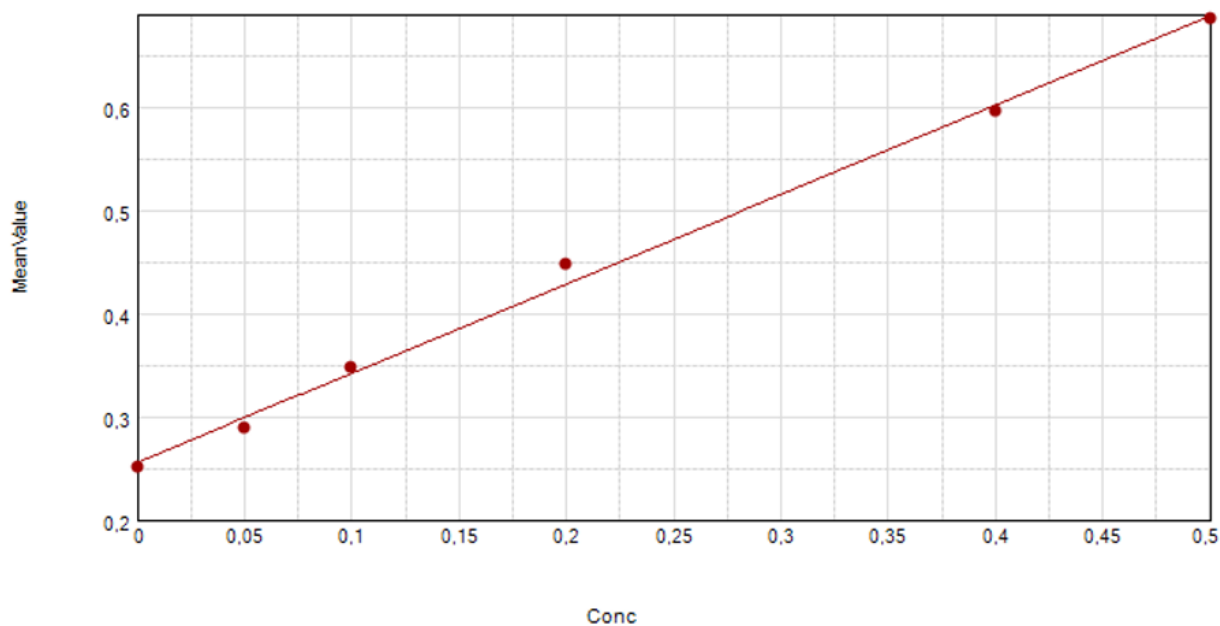
### **3.5 ITC**

Multiple ITC experiments were performed using both DYRK1A wt and DYRK1A C312A with the inhibitor Luciferin, with and without reductant present in the assay. Unfortunately, the results from the measurements were not reproducible and are thus not included in the thesis.

### **3.6 MST**

#### **3.6.1 Bradford assay**

The Bradford assay was used to verify the concentrations of DYRK1A and DYRK1A C312A. The standard curve can be seen underneath in Figure 14. The coefficient of determination (R<sup>2</sup>) was 0.996, which indicates highly accurate results. The standard line curve formula,  $y = A + Bx$  was used to calculate the concentrations (x) of the diluted protein. The concentrations of DYRK1A and DYRK1A C312A before dilution was found to be 10.64 mg/ml and 5.56 mg/ml, respectively.



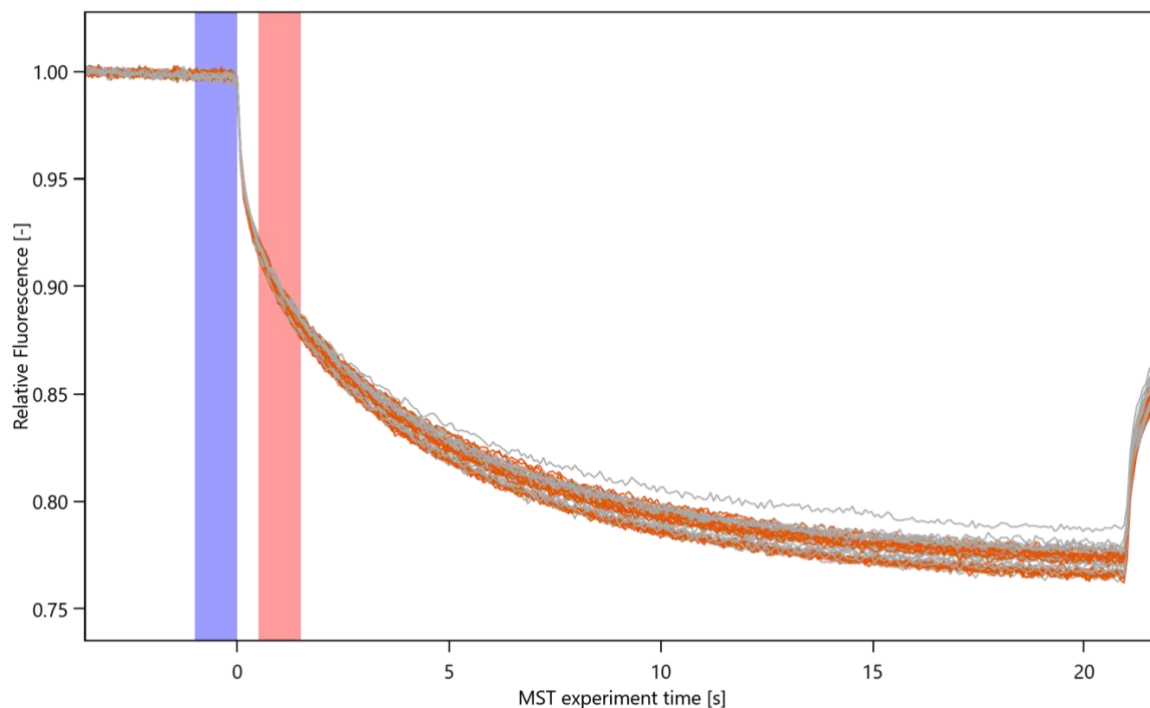
Curve Fit : Linear  $y = A + Bx$

	Parameter	Estimated Value	Std. Error	Confidence Interval
Std $R^2 = 0.996$	A	0.256	0.007	[0.236, 0.276]
	B	0.864	0.026	[0.791, 0.937]

**Figure 14: BSA standard curve created with the Bradford assay.** The standard curve line formula,  $y = A + Bx$ , was used to calculate the concentration (x) of the diluted protein. The concentrations of the protein before dilution were calculated to be 10.64 mg/ml for DYRK1A wt and 5.56 mg/ml for the mutant DYRK1A C312A.

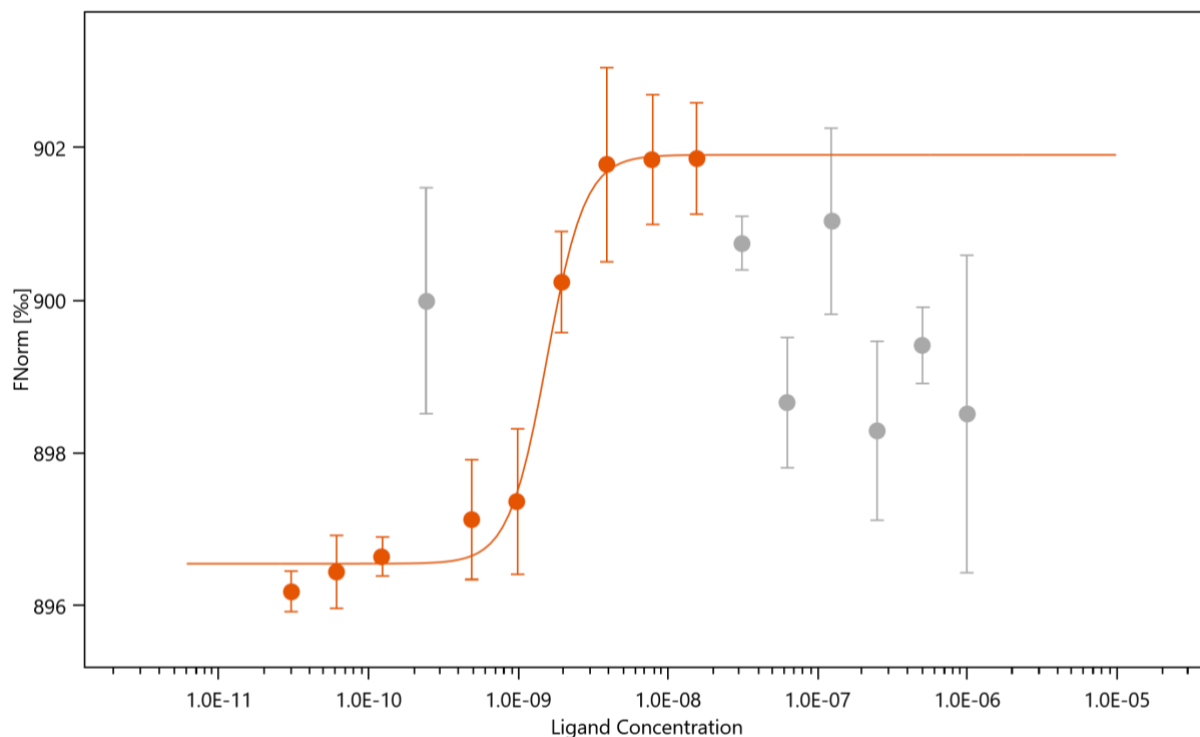
### 3.6.2 Binding assay

Figure 15 shows the traces produced from the 16 MST runs, with time (s) as the x-axis and relative fluorescence as the y-axis.



**Figure 15: Traces from the MST run.** This graph shows how the MST fluorescence signal varies over time. The x-axis is time (s) and the y-axis is relative fluorescence. The initial flat phase is detection of the sample fluorescence, which is commonly recorded for about 5 seconds. This is followed by activation of the MST power to induce the temperature gradient and subsequent detection of thermophoretic changes in fluorescence. Finally, MST power is deactivated, and back diffusion of fluorescent molecules is monitored. Outliers are shown in grey.

The results from each of the 16 individual MST runs were combined and averaged into a merge set, which can be seen underneath in Figure 16. Error bars have been calculated and are displayed in the figure. The x-axis is the ligand concentration (M), and the y-axis is the normalized fluorescence (%). An additional effect began to occur at higher peptide concentrations, possibly due to a second binding site. This data was thus removed from the analysis, along with an outlier at approximately 0.2 nM which was spurious. All outliers that were removed are represented as grey points in the graph. The data confirms that the peptide binds strongly to the mutant DYRK1A C312A, as is also the case for DYRK1A wt.



**Figure 16: MST merge set.** Data from the individual MST runs have been combined and averaged into a merge set. Error bars have been calculated and are displayed in the figure. The x-axis is the ligand concentration (M), and the y-axis is the normalized fluorescence (%). An additional effect began to occur at higher peptide concentrations, possibly due to a second binding site. This data was thus removed from the analysis, along with an outlier at approximately 0.2 nM which was spurious. All outliers that were removed are represented as grey points in the graph.

Results for capillary scan and shape can be found in the Appendix.

## 3.7 Crystallography

### 3.7.1 Crystallization and data collection

#### 3.7.1.1 *DYRK1A wt*

The crystallization conditions that resulted in the best diffracting crystals for *DYRK1A wt* with STU was 25% polyethylene glycol 3350 (PEG 3350), 0.2 M sodium acetate (NaAc) and 0.1 M Bis(2-hydroxyethyl)amino-tris(hydroxymethyl)methane (BisTris) pH 5.5. The crystals could be observed as early as two or three days after the crystallization trials were performed.

The diffracting crystals were all shaped like needles, as can be seen in Figure 17. They continued to grow noticeably in size for a few days. They were harvested with LV oil as a cryoprotectant and stored in nitrogen until the X-ray data collection.

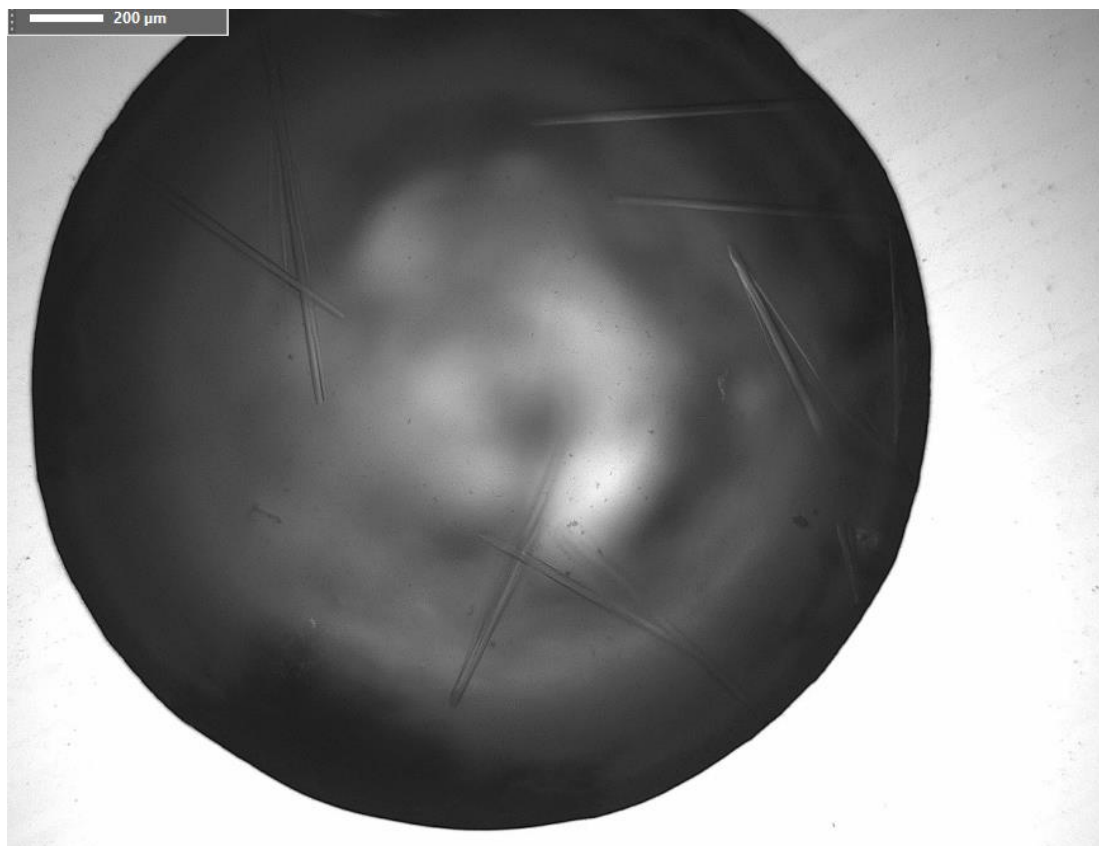


**Figure 17: Crystals of DYRK1A wt in complex with STU.** The drop contains 25% PEG 3350, 0.2 M sodium acetate (NaAc) and 0.1 M BisTris pH 5.5. The picture is taken 10 days after crystallization trials.

### **3.7.1.2 *DYRK1A C312A***

The crystallization conditions that resulted in the best diffracting crystals for the DYRK1A C312A mutant with STU was 0.1 M potassium chloride (KCl), 0.1 M potassium thiocyanate (KSCN) and 15.3% PEG 3350. The mutant also crystallized readily with higher concentrations of PEG 3350, and with 0.1 M NaCl or 0.1 M LiCl as alternatives to KCl. The crystals appeared as soon as the day after the crystallization trials and in a different shape than what was observed for the wt. Figure 18 shows a photo of the crystals, taken 10 days after crystallization trials.

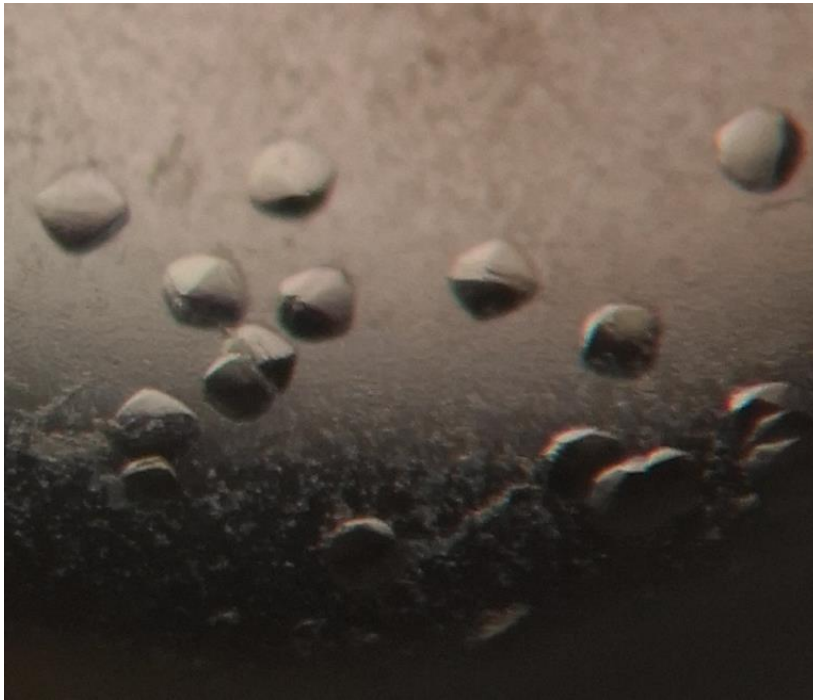


**Figure 18: Crystals of DYRK1A C312A in complex with STU.** The drop contains 0.1 M potassium chloride (KCl), 0.1 M potassium thiocyanate (KSCN) and 15.3% PEG 3350. The picture is taken 10 days after crystallization trials.

## 3.7.2 Crystal structures

### 3.7.2.1 *DYRK1A wt in complex with STU*

The DYRK1A wt crystallized with STU at a resolution of 2.34 Å. Diffraction images from two different angles can be seen in Figure 19.

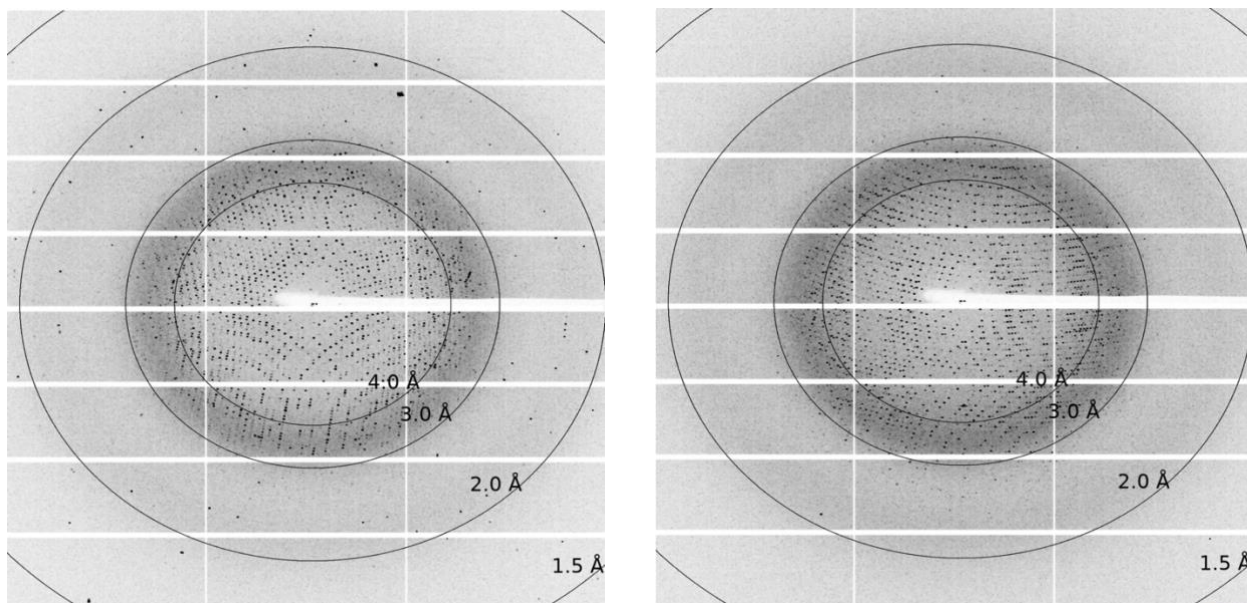


**Figure 19: Diffraction images of DYRK1A wt in complex with STU.**

The asymmetric unit of the wt comprises of two distinct monomers and is shown below in Figure 20. The space group of the wt is P63.

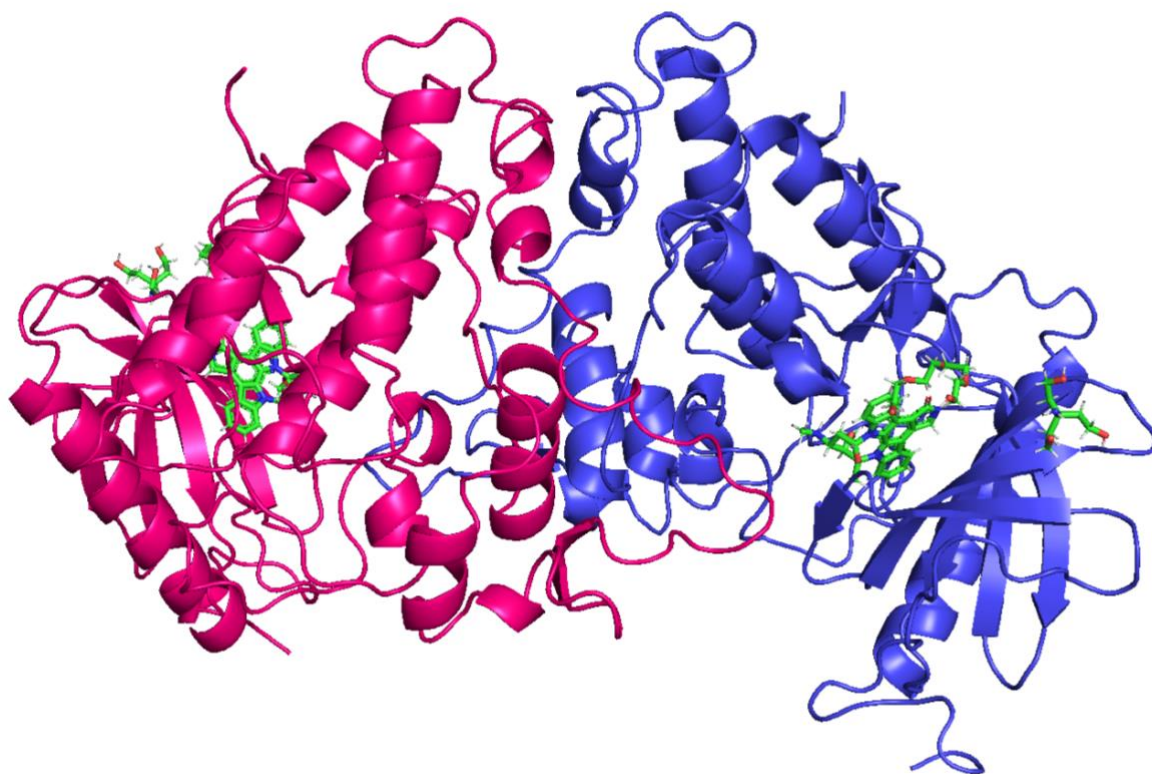


**Figure 20: The asymmetric unit of DYRK1A wt, comprising of two distinct monomers at 2.33 Å resolution.** The two monomers are colored differently in the figure.

Data and refinement statistics produced by Molprobity are listed in Table 8.

**Table 8: Data and refinement statistics for DYRK1A wt in complex with STU.** The data was calculated by Molprobity. (115)

Property	Value	Source
Space group	P63	Depositor
Cell constants	132.57Å 132.57Å 91.27Å	Depositor
a, b, c, $\alpha$ , $\beta$ , $\gamma$	90.00° 90.00° 120.00°	
Resolution (Å)	43.39 – 2.33	Depositor
	43.39 – 2.33	EDS
% Data completeness (in resolution range)	99.7 (43.49 – 2.33)	Depositor
	99.8 (43.39 – 2.33)	EDS
R <sub>merge</sub>	Not available	Depositor
R <sub>Sym</sub>	Not available	Depositor
$\langle I/\sigma(I) \rangle$	1.52 (at 2.34 Å)	Xtriage
Refinement program	Phenix.refine 1.14_3260, PHENIX 1.14_3260	Depositor
R, R <sub>free</sub>	0.194 , 0.248	Depositor
	0.194 , 0.247	DCC
R <sub>free</sub> test set	1071 reflectios (2.76%)	wwPDB-VP
Wilson B-factor (Å <sup>2</sup> )	45.6	Xtriage
Anisotropy	0.170	Xtriage
Bulk solvent k <sub>sol</sub> (e/Å <sup>3</sup> ), B <sub>sol</sub> (Å <sup>2</sup> )	0.33 , 37.1	EDS
L-test for twinning	$\langle  L  \rangle = 0.51$ , $\langle L^2 \rangle = 0.34$	Xtriage
Estimated twinning fraction	0.035 for h, -h-k, -l	Xtriage
F <sub>o</sub> , F <sub>c</sub> correlation	0.95	EDS
Total number of atoms	6026	wwPDB-VP
Average B, all atoms (Å <sup>2</sup> )	54.0	wwPDB-VP

### 3.7.2.2 *DYRK1A C312A in complex with STU*

The mutant DYRK1A C312A crystallized with STU at a resolution of 2.59 Å. The diffraction images used to determine the plan for data collection are shown underneath in Figure 21. The two images are taken 90° apart.

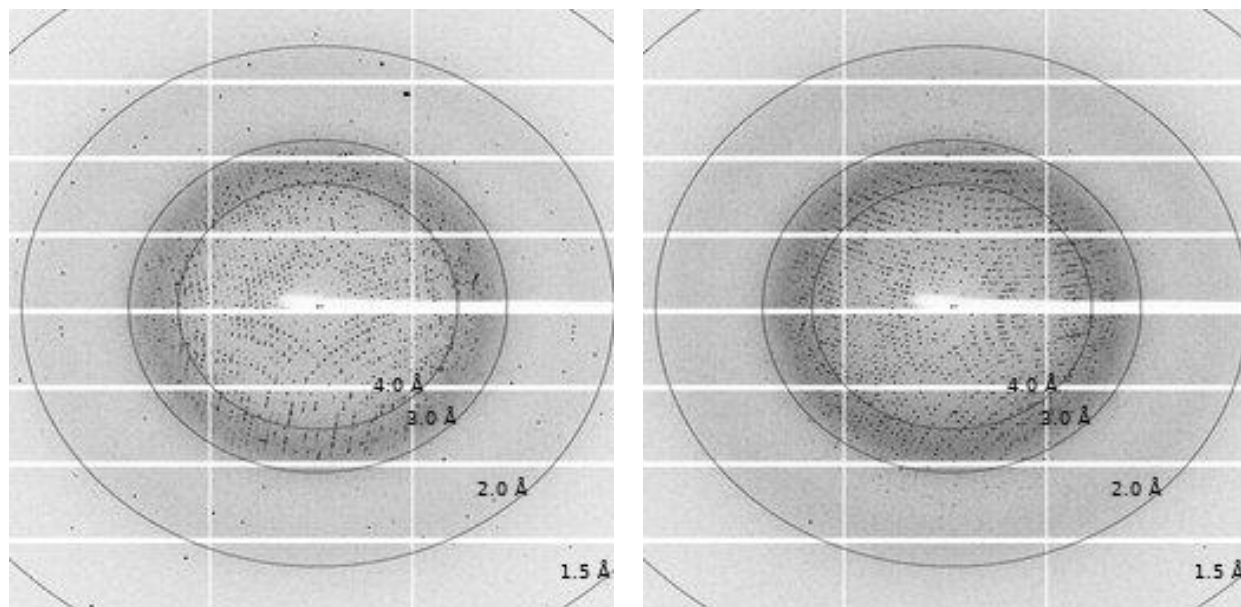


**Figure 21: Diffraction images of DYRK1A wt in complex with STU.**

The asymmetric unit of the mutant comprises of eight distinct monomers and is shown below in Figure 22. The space group of the mutant is P 31 2 1.

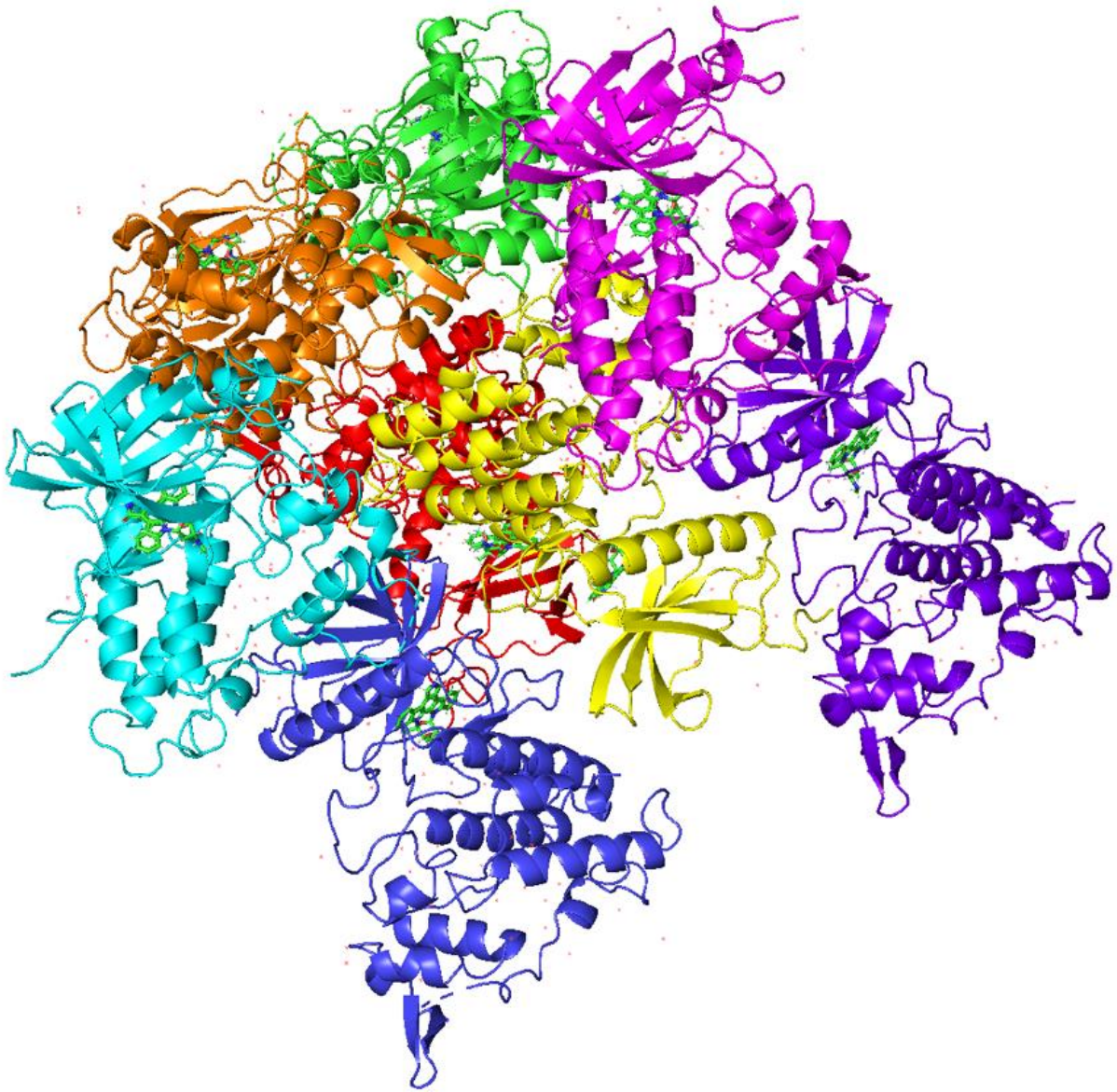


**Figure 22: The asymmetric unit of DYRK1A wt, comprising of eight distinct monomers at 2.59 Å resolution.** Each of the eight monomers is colored differently in the figure for better comprehension.

Data and refinement statistics produced by Molprobit are listed in Table 9.

**Table 9: Data and refinement statistic for DYRK1A C312A in complex with STU.** The data was calculated by Molprobity.(115)

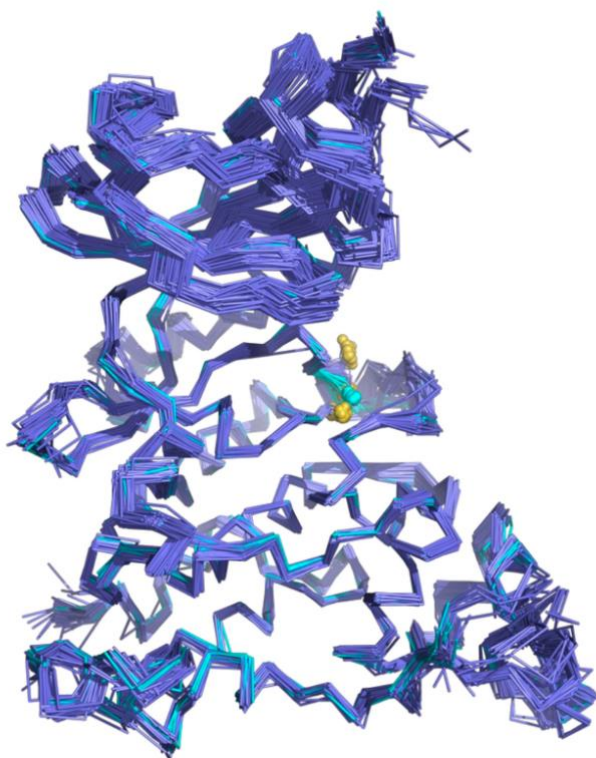
Property	Value	Source
Space group	P 31 2 1	Depositor
Cell constants	200.70Å 200.70Å 138.36Å	Depositor
a, b, c, $\alpha$ , $\beta$ , $\gamma$	90.00° 90.00° 120.00°	
Resolution (Å)	45.52 – 2.59	Depositor
	45.54 – 2.59	EDS
% Data completeness (in resolution range)	97.2 (45.52 – 2.59)	Depositor
	97.2 (45.52 – 2.59)	EDS
R <sub>merge</sub>	(Not available)	Depositor
R <sub>Sym</sub>	(Not available)	Depositor
< I/ $\sigma$ (I) >	1.21 (at 2.58 Å)	Xtrriage
Refinement program	phenix_refine 1.14_3260, PHENIX 1.14_3260	Depositor
R, R <sub>free</sub>	0.217 , 0.274	Depositor
	0.218 , 0.272	DCC
R <sub>free</sub> test set	2099 reflections (2.17%)	wwPDB-VP
Wilson B-factor (Å <sup>2</sup> )	40.6	Xtrriage
Anisotropy	0.138	Xtrriage
Bulk solvent k <sub>sol</sub> (e/Å <sup>3</sup> ), B <sub>sol</sub> (Å <sup>2</sup> )	0.36 43.9	EDS
L-test for twinning	<  L  > = 0.50, < L <sup>2</sup> > = 0.33	Xtrriage
Estimated twinning fraction	0.008 for -h, -k, l	Xtrriage
F <sub>o</sub> , F <sub>c</sub> correlation	0.93	EDS
Total number of atoms	23040	wwPDB-VP
Average B, all atoms (Å <sup>2</sup> )	44.0	wwPDB-VP

## 4 DISCUSSION

### 4.1 Superposition of structures

#### 4.1.1 Superposition of DYRK1A structures

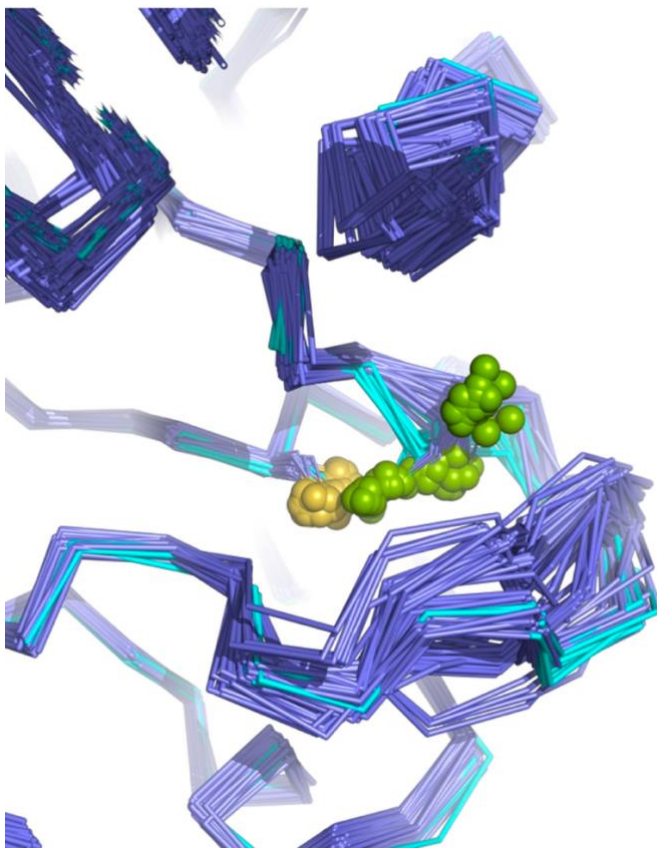
76 crystal structures of DYRK1A were superimposed using the “align” function in Pymol. Entry ID and PubMed ID for each of the structures is listed in Table 10 in Appendix. Figure 23 shows ribbon plots for all the aligned structures, with the two cysteines involved in disulfide bond formation (C286 and C312) in the middle right, colored yellow. The steel blue indicates that the structure has an open bridge, while cyan indicates that the structure has a closed bridge. The largest structural differences occur in the hinge region of the N-lobe. There is also a lot of variability in the AL near the two cysteines.



**Figure 23: Superposition of 76 crystal structures of DYRK1A.** The steel blue indicates that the structure has an open bridge, while cyan indicates that the structure has a closed bridge. The two cysteines are represented by yellow spheres. The figure was provided by Professor Richard Engh.

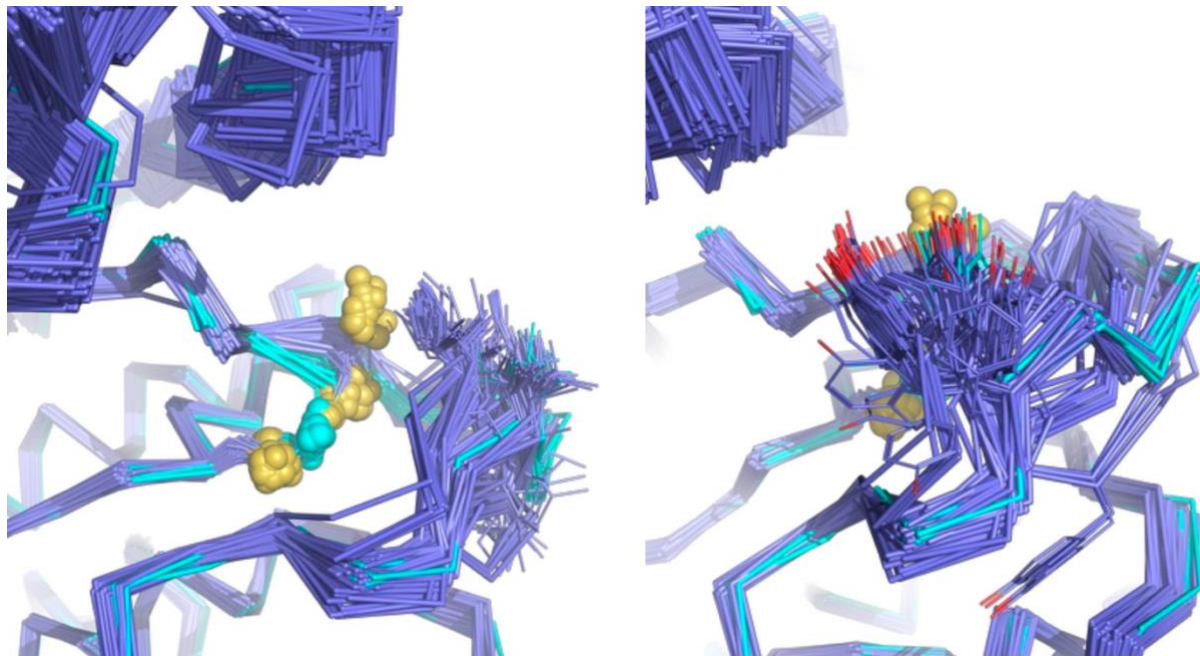
### 4.1.2 Activation loop structural variability

A closer look at the two cysteines involved in disulfide bridge formation is shown in Figure 24, offering insight into how the AL structures cluster. Cys286 is represented by yellow spheres, while Cys312 is represented by green spheres. Cys312, which is part of the DFGSSC sequence, shows greater structural variability than Cys286, which stays in a tight cluster independent of the state of the bridge. While some of the open bridge structures indicate that sulfurs of the cysteines to be almost in the same position as where it is when the bridge is closed, others show the side chain pointing away from Cys286, which leads to a shift in the position of the main chain, further affecting the variability of the activation loop (AL) geometries.



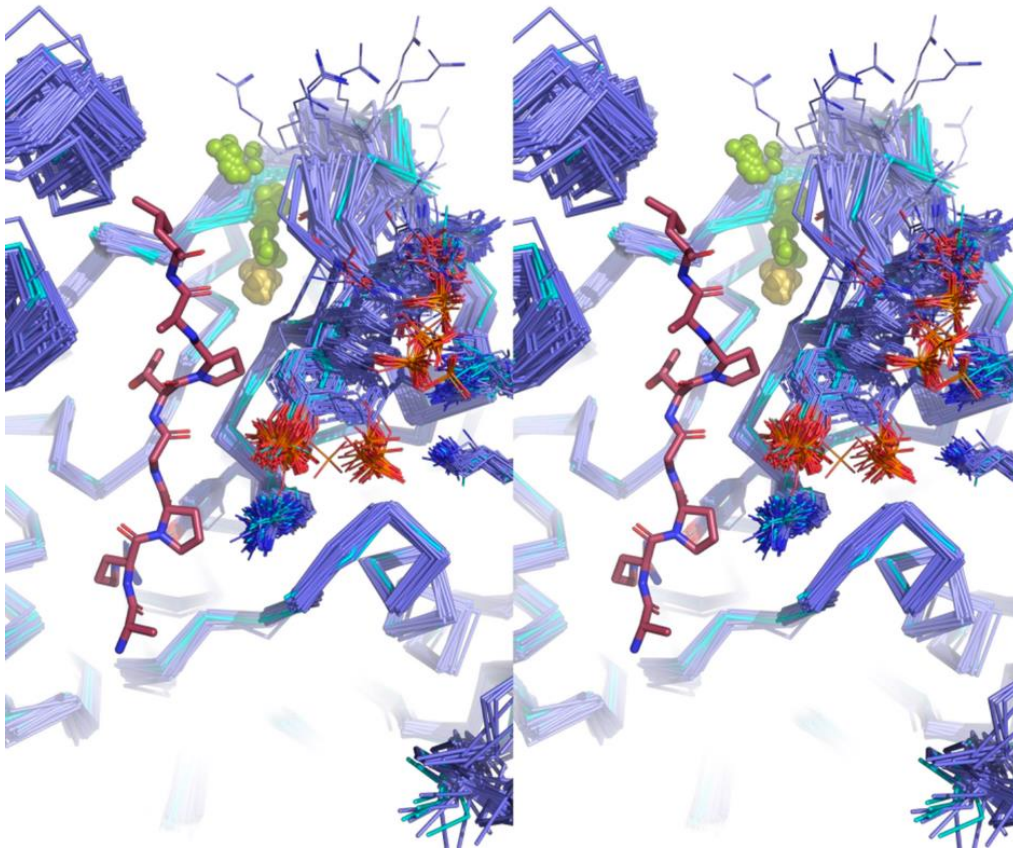
**Figure 24: Close-up of the two cysteines and the activation loop.** Cys286 of the HCD motif is represented by yellow spheres, whereas Cys312 of the DFGSSC sequence is represented by green spheres. The figure was provided by Professor Richard Engh.

Figure 25 shows how structural variations could possibly impact substrate binding. For instance, variations of the position of the phosphate group of Tyr321 may influence binding of the first residue C- terminal to the phosphorylation site.



**Figure 25: Closeup of the AL.** The figure shows structural variations of the AL. The figure was provided by Professor Richard Engh.

Variations of the AL positions creates many possibilities for binding of substrates further C-terminal to the phosphorylation site, which could possibly affect the redox sensitive substrate selectivity. Because the C helix plays a key role in stabilizing the catalytic geometry, changes in the interactions it is involved in have the potential to influence catalytic activity.



**Figure 26: Superposition of DYRK structures.** The figure illustrates how variations of the AL positions creates many possibilities for substrate binding further C-terminal to the phosphorylation site. The figure was provided by Professor Richard Engh.

#### 4.1.3 Superposition with the DYRK1A C312A mutant structures

Superposition of the eight monomers of the DYRK1A C312A mutant with the superposition of the 194 DYRK1A structures from the PDB is shown below in Figure 27. The C312A mutant structures are represented by black chains. Green chains indicate that the disulfide bridge between C286 and C312 is closed, and cyan chains indicate a unique configuration of the activation loop. The remaining chains are colored differently due to variations in the C-helix position. The activation loop conformation for C312A matches one of the clusters of open bridge conformations of the wild type structures.

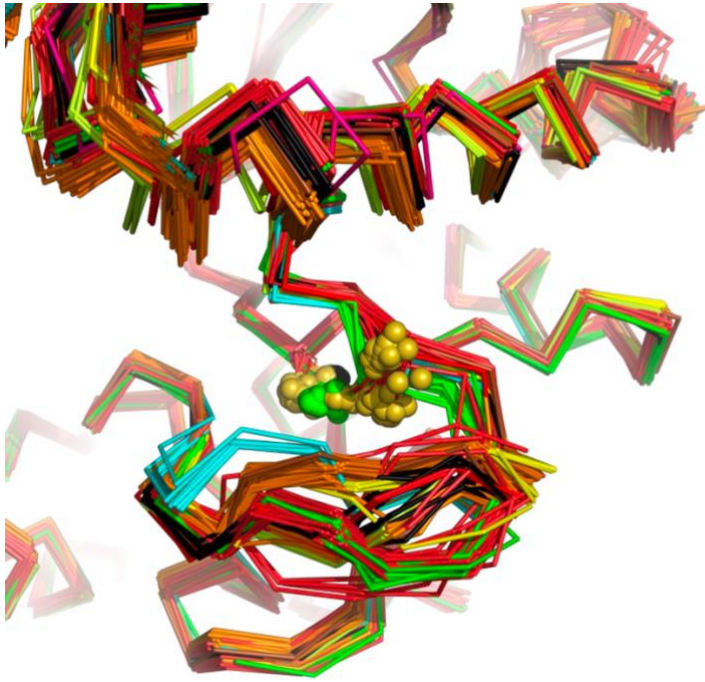


**Figure 27: Superposition of the eight monomers of the DYRK1A C312A mutant with the superposition of the 194 DYRK1A structures from the PDB.** The C312A mutant structures are represented by black chain. Green chains indicate that the disulfide bridge between C286 and C312 is closed. Cyan chains indicate a unique configuration of the activation loop. The figure is provided by Professor Richard Engh.

## 4.2 Thermofluor: Effects of oxidant/reductant on melting temperature

Interestingly, the results from the thermofluor assay show that while DYRK1A wt is stabilized by approximately 6°C after the addition of BME, DYRK1A C312A is destabilized by approximately 5°C. BME is a reductant and consequently one would expect that it reduces (opens) the HCD-DFGSSC disulfide bridge. If that is the case, then the notion that a closed bridge increases stability would be wrong. Since there is no disulfide bridge in the mutant, the addition of a reductant was not expected to have an impact on the melting temperature of the protein, which makes it difficult to explain the significant decrease in melting temperature for the apo protein.

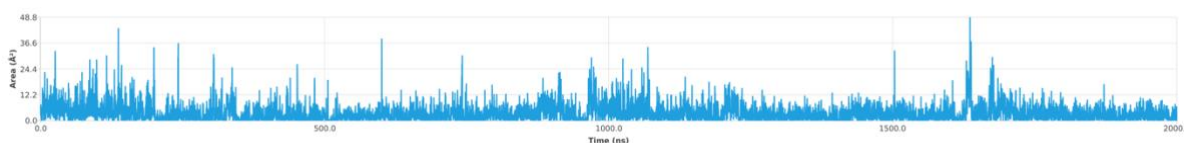
Ligand binding seemingly has a much greater effect on the mutant than the wt. Because air oxidation might take place, it is impossible to know whether the untreated protein is still in a reduced state or not. The mutant undoubtedly has no disulfide bridge, which indicates that the

absence of the bridge leads to an increase in the flexibility of the AL and consequently a decrease in stability. This seems, however, to be restored upon inhibitor binding.

### 4.3 Molecular dynamics: Does MD hint at accessibility to conserved cysteine residues?

The solvent accessible surface area (SASA) of a molecule is a quantitative measure of the contact area between the molecule and the solvent. The relation between SASA and free energy is somewhat ambiguous, however it is a useful tool for comparing molecules of different conformations, as well as measuring the surface area that is buried as a result of oligomerization. (116) SASA for the two cysteines involved in disulfide bridge formation in DYRK1A is shown as a function of time in Figure 28.

Cys 286



Cys 312

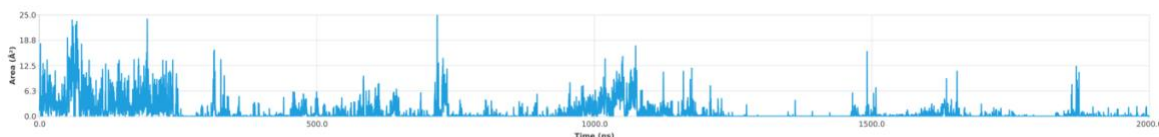


**Figure 28: Solvent accessible surface area (SASA) for Cys 286 and Cys 312.**

The SASA for the two cysteines involved in the disulfide bridge formation at HCD-DFGSSC is of particular interest because the bridge may function as a redox sensitive switch. If so, the accessibility of the cysteine side chains may be important for chemical reactions, such as interactions with reactants that are involved in disulfide bridge regulation. SASA for the cysteines is also interesting in terms of covalent inhibition strategies. It is evident from Figure 28 that the two cysteines behave very differently in terms of SASA. Cys286, which is part of the HCD motif, has considerable accessibility all throughout the 2  $\mu$ s MD trajectory. There are also several spikes of high accessibility for this cysteine residue. This is not the case for Cys312, part of the DFGSSC motif, which has moderate accessibility at the start but then drops to a low accessibility which it maintains for the rest of the run, with only a few

occasional spikes of moderate accessibility. This is an interesting observation, as one would expect Cys286, which is located in the flexible AL, to exhibit larger changes due to movement which would affect the interactions determining the solvent accessibility.

The distance between the sulfur atoms on Cys286 and Cys312 is plotted in Figure 29, and interestingly the spikes at 300 ns, 1100 ns and 1500 ns seem to be related to spikes in the two SASA plots occurring at the same time. To illustrate this, a close-up of the spike at 1500 ns for each of the three plots are lined up in Figure 30. This correlation indicates that as the cysteines move further apart from each other, they become more exposed to the solvent.

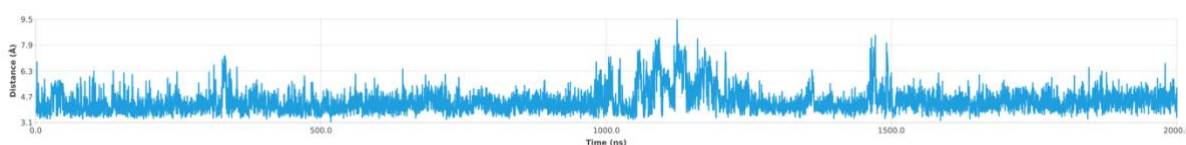


**Figure 29: Distances between the sulfur atom on C286 and the sulfur atom on C312 as a function of time.**

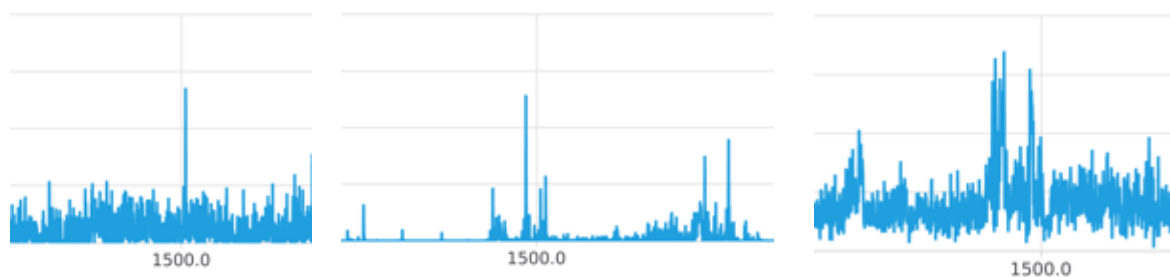


**Figure 30: Close-up of the spikes at 1500 ns occurring in the SASA plots for C286 and C312, and the plot of the distance between the sulfurs on the two cysteines.** This indicates that an increase in the distance between the two cysteines leads to them being more exposed to the solvent.

Other interesting distances that were measured include the hydrogen bond between residues Q199 and Y319, which is only found in a few of the X-ray structures. The plot of the distances can be seen in Figure 31 underneath. There is a big spike in the beginning of the trajectory, indicating a large increase in the distance between the two residues resulting in a breaking of the bond. However, shortly after they find their way back to one another and remain stable for the remainder of the trajectory. This is surprising, as one would expect from looking at the X-ray structures, that the bond would be highly unstable.

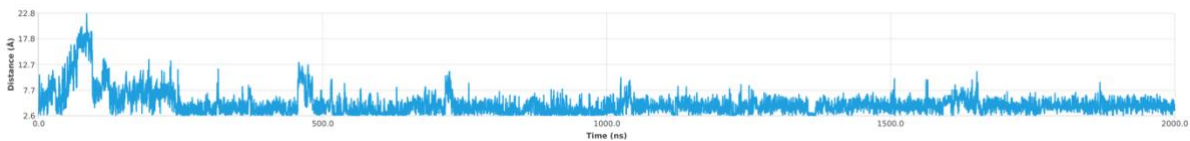


**Figure 31: Distances of the hydrogen bond between Q199 and Y319.** There is a large increase in the distance between residues Q199 and Y319 in the beginning of the trajectory. However, it decreases soon after and remains stable for the rest of the trajectory. This is not what one would expect from looking at the X-ray structures.

Distance plots of other interesting interactions, such as the phosphate anchoring and the distance between the Gly-loop and the C-helix can be found in Appendix.

## **FUTURE WORK**

It would be interesting to crystallize DYRK1A and the mutant DYRK1A C312A with other inhibitors, especially ones that have shown potential for therapeutic effects, such as drug candidates for Alzheimer disease. It would also be good to perform new ITC experiments, as this would produce results for enthalpy and binding constants, which would further allow for the calculation of entropy.

## SUMMARY

The cysteine of HCD (C286) in DYRK1A is involved in disulfide bridge formation with a cysteine (C312) in the DFGSSC sequence. The purpose of this project was to investigate how the state of the disulfide bridge would affect enzyme catalytic and ligand binding properties of the protein kinase. A mutant, DYRK1A C312A, was thus designed to eliminate the disulfide bridge. The mutant was expressed and purified following the same protocol as for DYRK1A wt, including HisTrap purification, TEV cleavage and size exclusion chromatography. Crystallization trials were performed for both the wt and the mutant with the kinase inhibitor Staurosporine. DYRK1A wt with STU crystallized and diffracted with at a resolution of 2.33 Å. The DYRK1A C312A mutant with STU crystallized and diffracted with a resolution of 2.59 Å. The structure was solved by molecular replacement in Molrep (CCP4) and refined by Refmac5 and Phenix. Molecular dynamics (MD) simulations (SCHRODINGER) were performed with the intent to compare diverse disulfide bridge states. Ligand binding and enzyme catalytic properties were analyzed using a combination of techniques, including activity assays, microscale thermophoresis, and isothermal calorimetry. The Thermofluor assay confirmed that both the wt and the mutant bind tightly to STU and AZ-191. It also showed that the mutant consistently has a slightly lower melting temperature than the wt, which would indicate that it is less stable. Solvent accessible surface area (SASA) analysis support the theory of accessibility to conserved cysteine residues.

## APPENDIX

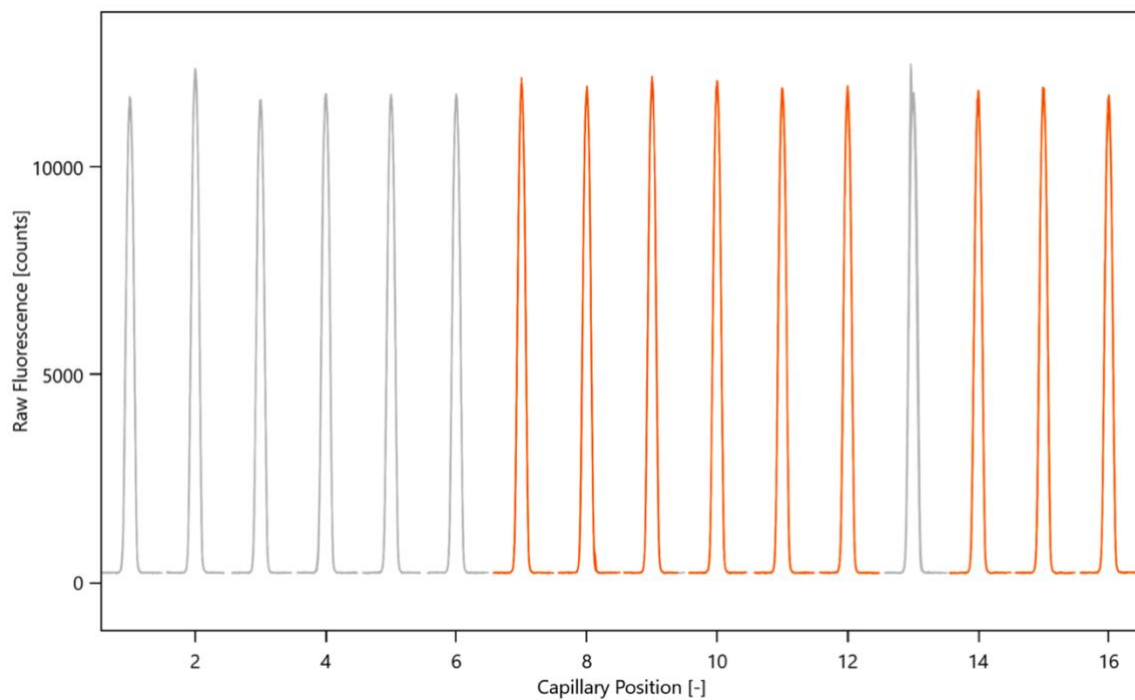


**Figure 32: MST Capillary scan**

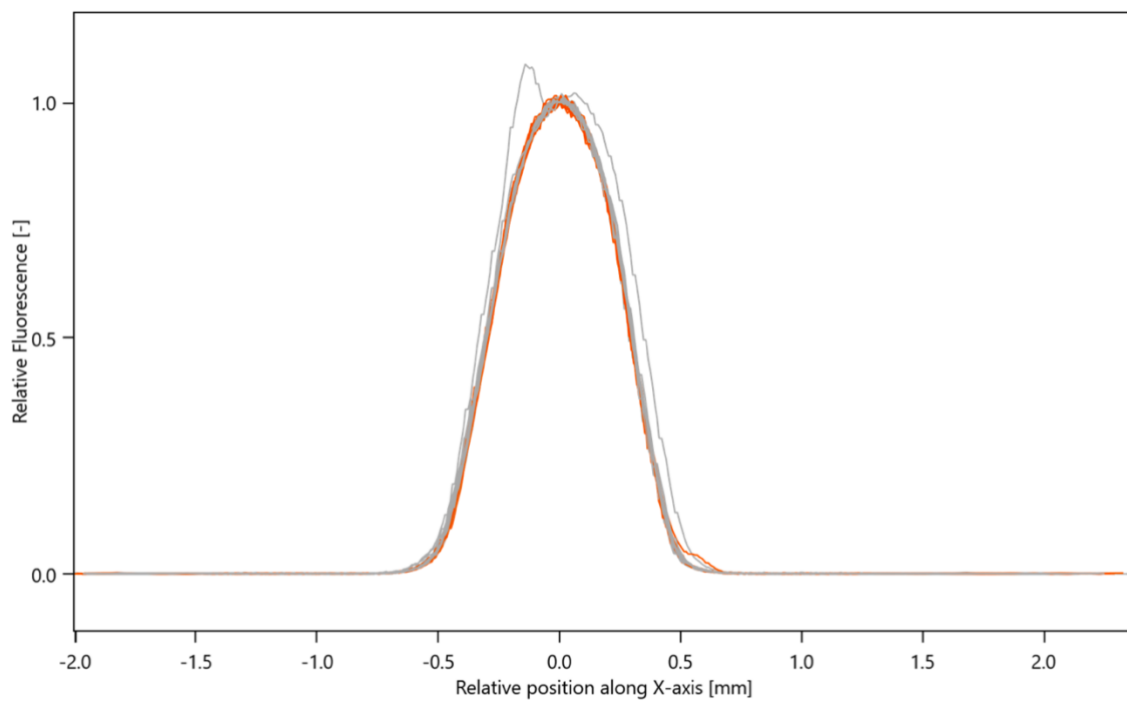


**Figure 33: MST Capillary shape**

**Table 10: Entry ID and PubMed ID for DYRK1A structures used in structure alignment.**

<b>Entry ID</b>	<b>PubMed ID</b>
2VX3 <sup>(117)</sup>	23665168
2WO6 <sup>(117)</sup>	23665168
3ANQ <sup>(118)</sup>	20981014
3ANR <sup>(118)</sup>	20981014
4AZE <sup>(119)</sup>	22998443
4MQ1 <sup>(120)</sup>	24239188
4MQ2 <sup>(120)</sup>	24239188
4NCT <sup>(8)</sup>	25945585
4YLJ <sup>(121)</sup>	25730262
4YLK <sup>(121)</sup>	25730262
4YLL <sup>(121)</sup>	25730262
4YU2 <sup>(122)</sup>	33339338
5A3X <sup>(123)</sup>	27736065
5A4E <sup>(123)</sup>	27736065
5A4L <sup>(123)</sup>	27736065
5A4Q <sup>(123)</sup>	27736065
5A4T <sup>(123)</sup>	27736065
5A54 <sup>(123)</sup>	27736065
5AIK	
6A1F <sup>(124)</sup>	30217414
6A1G <sup>(124)</sup>	30217414
6EIF <sup>(125)</sup>	30095246
6EIJ <sup>(125)</sup>	30095246
6EIL <sup>(125)</sup>	30095246
6EIP <sup>(125)</sup>	30095246
6EIQ <sup>(125)</sup>	30095246
6EIR <sup>(125)</sup>	30095246
6EIS <sup>(125)</sup>	30095246
6EIV <sup>(125)</sup>	30095246
6EJ4 <sup>(125)</sup>	30095246
6LN1 <sup>(126)</sup>	34323401
6QU2	
6S11	
6S14	
6S17	
6S1B	
6S1H	
6S1I <sup>(127)</sup>	32832032
6S1J	
6T6A <sup>(128)</sup>	31766108
6UIP <sup>(129)</sup>	32077280
6UWY <sup>(130)</sup>	32003560
6YF8	
7A4O <sup>(131)</sup>	34143631

---

7A4R <sup>(131)</sup>	34143631
7A4S <sup>(131)</sup>	34143631
7A4W <sup>(131)</sup>	34143631
7A4Z <sup>(131)</sup>	34143631
7A51 <sup>(131)</sup>	34143631
7A52 <sup>(131)</sup>	34143631
7A53 <sup>(131)</sup>	34143631
7A55 <sup>(131)</sup>	34143631
7A5B <sup>(131)</sup>	34143631
7A5D <sup>(131)</sup>	34143631
7A5L <sup>(131)</sup>	34143631
7A5N <sup>(131)</sup>	34143631
7AJ2 <sup>(132)</sup>	33975430
7AJ4 <sup>(132)</sup>	33975430
7AJ5 <sup>(132)</sup>	33975430
7AJ7 <sup>(132)</sup>	33975430
7AJ8 <sup>(132)</sup>	33975430
7AJA <sup>(132)</sup>	33975430
7AJM <sup>(132)</sup>	33975430
7AJS <sup>(132)</sup>	33975430
7AJV <sup>(132)</sup>	33975430
7AJW <sup>(132)</sup>	33975430
7AJY <sup>(132)</sup>	33975430
7AK2 <sup>(132)</sup>	33975430
7AKA <sup>(132)</sup>	33975430
7AKB <sup>(132)</sup>	33975430
7AKE <sup>(132)</sup>	33975430
7AKL <sup>(132)</sup>	33975430
7FHS <sup>(133)</sup>	34742017
7FHT <sup>(133)</sup>	34742017
7O7K <sup>(134)</sup>	34785661
7OY6 <sup>(135)</sup>	34959172

---

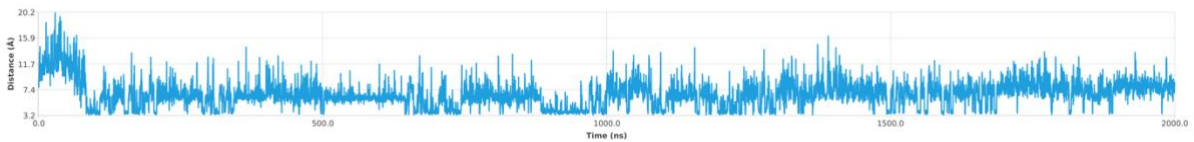


**Figure 34: K939-P distance**

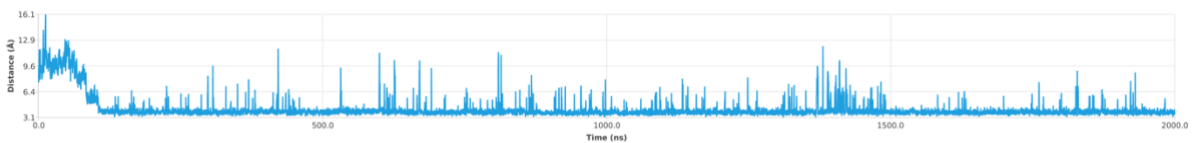


**Figure 35: K390-P distance**

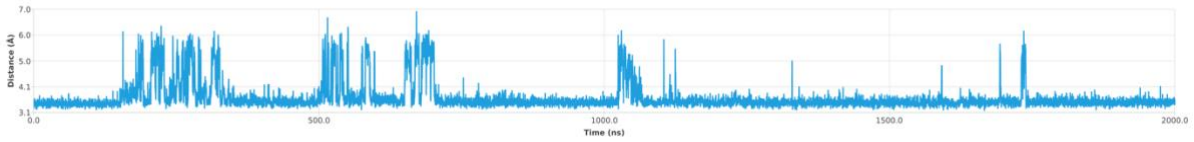


**Figure 36: K188-E203 distance**

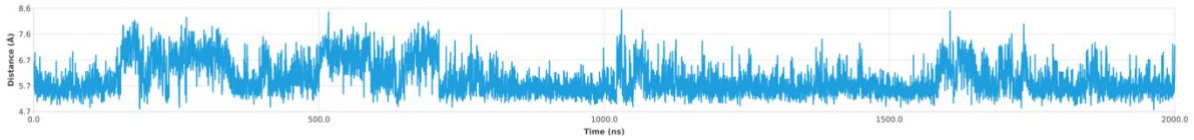


**Figure 37: Glycine rich loop-Phe STU distance**

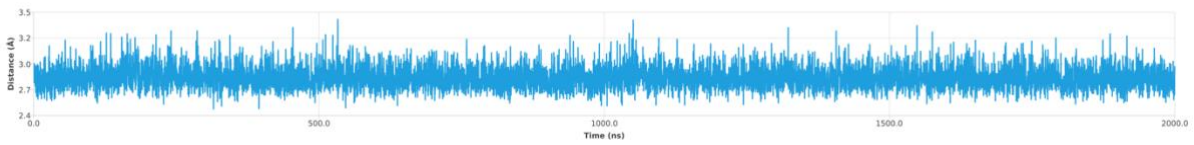


**Figure 38: GK+3 STU H-bond distance**

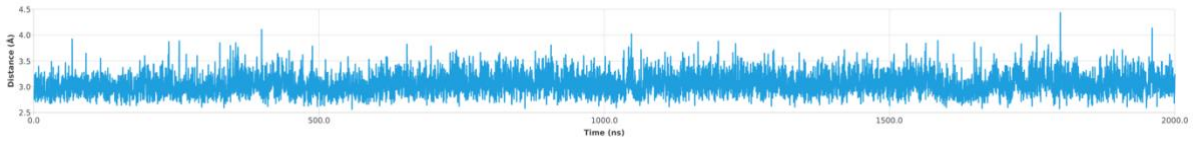


**Figure 39: GK+1 STU H-bond distance**

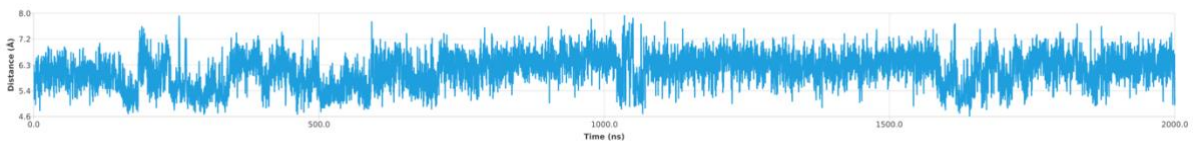


**Figure 40: GK- STU ring distance**

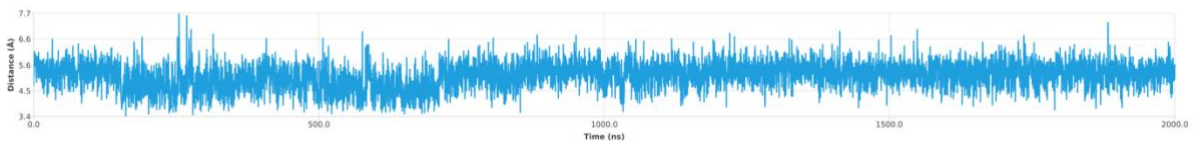


**Figure 41: F170 Glycine rich loop- F196 Helix C**

## REFERENCES

1. Chen J, Li Y, Du C, Wei T, Shan T, Wang L. Protein kinases in cardiovascular diseases. *Chin Med J (Engl)*. 2022;135(5):557-70.
2. Kanev GK, de Graaf C, de Esch IJP, Leurs R, Würdinger T, Westerman BA, et al. The Landscape of Atypical and Eukaryotic Protein Kinases. *Trends Pharmacol Sci*. 2019;40(11):818-32.
3. Duong-Ly KC, Peterson JR. The human kinome and kinase inhibition. *Curr Protoc Pharmacol*. 2013;Chapter 2:Unit2.9.
4. Manning G, Whyte DB, Martinez R, Hunter T, Sudarsanam S. The protein kinase complement of the human genome. *Science*. 2002;298(5600):1912-34.
5. Shen K, Hines AC, Schwarzer D, Pickin KA, Cole PA. Protein kinase structure and function analysis with chemical tools. *Biochim Biophys Acta*. 2005;1754(1-2):65-78.
6. Miller CJ, Turk BE. Homing in: Mechanisms of Substrate Targeting by Protein Kinases. *Trends Biochem Sci*. 2018;43(5):380-94.
7. The PyMOL Molecular Graphics System, Version 2.0 Schrödinger, LLC. [
8. Alexeeva M, Aberg E, Engh R, Rothweiler U. The structure of a dual-specificity tyrosine phosphorylation-regulated kinase 1A–PKC412 complex reveals disulfide-bridge formation with the anomalous catalytic loop HRD(HCD) cysteine. *Acta Crystallographica Section D Biological Crystallography*. 2015;71.
9. Taylor SS, Keshwani MM, Steichen JM, Kornev AP. Evolution of the eukaryotic protein kinases as dynamic molecular switches. *Philos Trans R Soc Lond B Biol Sci*. 2012;367(1602):2517-28.
10. Gógl G, Kornev AP, Reményi A, Taylor SS. Disordered Protein Kinase Regions in Regulation of Kinase Domain Cores. *Trends Biochem Sci*. 2019;44(4):300-11.
11. Meharena HS, Chang P, Keshwani MM, Oruganty K, Nene AK, Kannan N, et al. Deciphering the structural basis of eukaryotic protein kinase regulation. *PLoS Biol*. 2013;11(10):e1001680.
12. Yeung W, Ruan Z, Kannan N. Emerging roles of the  $\alpha$ C- $\beta$ 4 loop in protein kinase structure, function, evolution, and disease. *IUBMB Life*. 2020;72(6):1189-202.
13. Schwarz D, Merget B, Deane C, Fulle S. Modeling conformational flexibility of kinases in inactive states. *Proteins*. 2019;87(11):943-51.
14. Oruganty K, Talathi NS, Wood ZA, Kannan N. Identification of a hidden strain switch provides clues to an ancient structural mechanism in protein kinases. *Proc Natl Acad Sci U S A*. 2013;110(3):924-9.
15. Eswaran J, Knapp S. Insights into protein kinase regulation and inhibition by large scale structural comparison. *Biochim Biophys Acta*. 2010;1804(3):429-32.
16. Marcotte D, Rushe M, R MA, Lukacs C, Atkins K, Sun X, et al. Germinal-center kinase-like kinase co-crystal structure reveals a swapped activation loop and C-terminal extension. *Protein Sci*. 2017;26(2):152-62.
17. Umezawa K, Kii I. Druggable Transient Pockets in Protein Kinases. *Molecules*. 2021;26(3).
18. Kornev AP, Taylor SS, Ten Eyck LF. A helix scaffold for the assembly of active protein kinases. *Proc Natl Acad Sci U S A*. 2008;105(38):14377-82.
19. Taylor SS, Kornev AP. Protein kinases: evolution of dynamic regulatory proteins. *Trends Biochem Sci*. 2011;36(2):65-77.
20. Kornev AP, Taylor SS. Defining the conserved internal architecture of a protein kinase. *Biochim Biophys Acta*. 2010;1804(3):440-4.

21. Aranda S, Laguna A, de la Luna S. DYRK family of protein kinases: evolutionary relationships, biochemical properties, and functional roles. *Faseb j.* 2011;25(2):449-62.
22. Pastor F, Shkreta L, Chabot B, Durantel D, Salvetti A. Interplay Between CMGC Kinases Targeting SR Proteins and Viral Replication: Splicing and Beyond. *Front Microbiol.* 2021;12:658721.
23. Boni J, Rubio-Perez C, López-Bigas N, Fillat C, de la Luna S. The DYRK Family of Kinases in Cancer: Molecular Functions and Therapeutic Opportunities. *Cancers (Basel).* 2020;12(8).
24. Lindberg MF, Meijer L. Dual-Specificity, Tyrosine Phosphorylation-Regulated Kinases (DYRKs) and cdc2-Like Kinases (CLKs) in Human Disease, an Overview. *Int J Mol Sci.* 2021;22(11).
25. Soppa U, Becker W. DYRK protein kinases. *Curr Biol.* 2015;25(12):R488-9.
26. Lochhead PA, Sibbet G, Morrice N, Cleghon V. Activation-loop autophosphorylation is mediated by a novel transitional intermediate form of DYRKs. *Cell.* 2005;121(6):925-36.
27. Wegiel J, Gong CX, Hwang YW. The role of DYRK1A in neurodegenerative diseases. *Febs j.* 2011;278(2):236-45.
28. Park J, Chung KC. New Perspectives of Dyrk1A Role in Neurogenesis and Neuropathologic Features of Down Syndrome. *Exp Neurobiol.* 2013;22(4):244-8.
29. Becker W, Joost HG. Structural and functional characteristics of Dyrk, a novel subfamily of protein kinases with dual specificity. *Prog Nucleic Acid Res Mol Biol.* 1999;62:1-17.
30. Uniprot Available from <<http://www.uniprot.org> >
31. Jalview Available from <<http://www.jalview.org>>
32. Brown N, Leroy C, Sander C. MView: A web-compatible database search or multiple alignment viewer. *Bioinformatics (Oxford, England).* 1998;14:380-1.
33. Lee Walmsley D, Murray JB, Dokurno P, Massey AJ, Benwell K, Fiumana A, et al. Fragment-Derived Selective Inhibitors of Dual-Specificity Kinases DYRK1A and DYRK1B. *J Med Chem.* 2021;64(13):8971-91.
34. Lorenz R, Wu J, Herberg FW, Taylor SS, Engh RA. Drugging the Undruggable: How Isoquinolines and PKA Initiated the Era of Designed Protein Kinase Inhibitor Therapeutics. *Biochemistry.* 2021;60(46):3470-84.
35. Cohen P, Cross D, Jänne PA. Kinase drug discovery 20 years after imatinib: progress and future directions. *Nat Rev Drug Discov.* 2021;20(7):551-69.
36. Rowley JD. Letter: A new consistent chromosomal abnormality in chronic myelogenous leukaemia identified by quinacrine fluorescence and Giemsa staining. *Nature.* 1973;243(5405):290-3.
37. Shtivelman E, Lifshitz B, Gale RP, Canaani E. Fused transcript of abl and bcr genes in chronic myelogenous leukaemia. *Nature.* 1985;315(6020):550-4.
38. Turk BE. Understanding and exploiting substrate recognition by protein kinases. *Curr Opin Chem Biol.* 2008;12(1):4-10.
39. Zuccotto F, Ardini E, Casale E, Angiolini M. Through the "gatekeeper door": exploiting the active kinase conformation. *J Med Chem.* 2010;53(7):2681-94.
40. Kufareva I, Abagyan R. Type-II kinase inhibitor docking, screening, and profiling using modified structures of active kinase states. *J Med Chem.* 2008;51(24):7921-32.
41. Liu Y, Gray NS. Rational design of inhibitors that bind to inactive kinase conformations. *Nat Chem Biol.* 2006;2(7):358-64.
42. Baier A, Szyszka R. Compounds from Natural Sources as Protein Kinase Inhibitors. *Biomolecules.* 2020;10(11).

43. Yang Z, Hackshaw A, Feng Q, Fu X, Zhang Y, Mao C, et al. Comparison of gefitinib, erlotinib and afatinib in non-small cell lung cancer: A meta-analysis. *Int J Cancer*. 2017;140(12):2805-19.
44. Hanson SM, Georghiou G, Thakur MK, Miller WT, Rest JS, Chodera JD, et al. What Makes a Kinase Promiscuous for Inhibitors? *Cell Chem Biol*. 2019;26(3):390-9.e5.
45. Cortes JE, Kim DW, Pinilla-Ibarz J, le Coutre PD, Paquette R, Chuah C, et al. Ponatinib efficacy and safety in Philadelphia chromosome-positive leukemia: final 5-year results of the phase 2 PACE trial. *Blood*. 2018;132(4):393-404.
46. Nakano H, Omura S. Chemical biology of natural indolocarbazole products: 30 years since the discovery of staurosporine. *J Antibiot (Tokyo)*. 2009;62(1):17-26.
47. Meggio F, Donella Deana A, Ruzzene M, Brunati AM, Cesaro L, Guerra B, et al. Different susceptibility of protein kinases to staurosporine inhibition. Kinetic studies and molecular bases for the resistance of protein kinase CK2. *Eur J Biochem*. 1995;234(1):317-22.
48. ChemDraw Available from: <http://www.perkinelmer.co.uk/category/chemdraw>.
49. Disney AJ, Kellam B, Dekker LV. Alkylation of Staurosporine to Derive a Kinase Probe for Fluorescence Applications. *ChemMedChem*. 2016;11(9):972-9.
50. Millward MJ, House C, Bowtell D, Webster L, Olver IN, Gore M, et al. The multikinase inhibitor midostaurin (PKC412A) lacks activity in metastatic melanoma: a phase IIA clinical and biologic study. *British Journal of Cancer*. 2006;95(7):829-34.
51. Levis M. Midostaurin approved for FLT3-mutated AML. *Blood*. 2017;129(26):3403-6.
52. Prescher JA, Contag CH. Guided by the light: visualizing biomolecular processes in living animals with bioluminescence. *Curr Opin Chem Biol*. 2010;14(1):80-9.
53. Rothweiler U, Eriksson J, Stensen W, Leeson F, Engh RA, Svendsen JS. Luciferin and derivatives as a DYRK selective scaffold for the design of protein kinase inhibitors. *Eur J Med Chem*. 2015;94:140-8.
54. Tarrant MK, Cole PA. The chemical biology of protein phosphorylation. *Annu Rev Biochem*. 2009;78:797-825.
55. Becker W, Sippl W. Activation, regulation, and inhibition of DYRK1A. *Febs j*. 2011;278(2):246-56.
56. Bain J, McLauchlan H, Elliott M, Cohen P. The specificities of protein kinase inhibitors: an update. *Biochem J*. 2003;371(Pt 1):199-204.
57. Bain J, Plater L, Elliott M, Shpiro N, Hastie CJ, McLauchlan H, et al. The selectivity of protein kinase inhibitors: a further update. *Biochem J*. 2007;408(3):297-315.
58. Wang P, Alvarez-Perez JC, Felsenfeld DP, Liu H, Sivendran S, Bender A, et al. A high-throughput chemical screen reveals that harmine-mediated inhibition of DYRK1A increases human pancreatic beta cell replication. *Nat Med*. 2015;21(4):383-8.
59. Kumar K, Suebsuwong C, Wang P, Garcia-Ocana A, Stewart AF, DeVita RJ. DYRK1A Inhibitors as Potential Therapeutics for  $\beta$ -Cell Regeneration for Diabetes. *J Med Chem*. 2021;64(6):2901-22.
60. Barzowska A, Pucelik B, Pustelny K, Matsuda A, Martyniak A, Stepniewski J, et al. DYRK1A Kinase Inhibitors Promote  $\beta$ -Cell Survival and Insulin Homeostasis. *Cells*. 2021;10(9).
61. Vetere A, Choudhary A, Burns SM, Wagner BK. Targeting the pancreatic  $\beta$ -cell to treat diabetes. *Nat Rev Drug Discov*. 2014;13(4):278-89.
62. Forman HJ, Ursini F, Maiorino M. An overview of mechanisms of redox signaling. *J Mol Cell Cardiol*. 2014;73:2-9.
63. Sarsour EH, Kumar MG, Chaudhuri L, Kalen AL, Goswami PC. Redox control of the cell cycle in health and disease. *Antioxid Redox Signal*. 2009;11(12):2985-3011.

64. Lee BWL, Ghode P, Ong DST. Redox regulation of cell state and fate. *Redox Biol.* 2019;25:101056.
65. Meister A. Glutathione metabolism and its selective modification. *J Biol Chem.* 1988;263(33):17205-8.
66. Adeoye O, Olawumi J, Opeyemi A, Christiania O. Review on the role of glutathione on oxidative stress and infertility. *JBRA Assist Reprod.* 2018;22(1):61-6.
67. Ying W. NAD<sup>+</sup>/NADH and NADP<sup>+</sup>/NADPH in cellular functions and cell death: regulation and biological consequences. *Antioxid Redox Signal.* 2008;10(2):179-206.
68. Hershberger KA, Martin AS, Hirschey MD. Role of NAD(+) and mitochondrial sirtuins in cardiac and renal diseases. *Nat Rev Nephrol.* 2017;13(4):213-25.
69. Lee H, Torres J, Truong L, Chaudhuri R, Mittal A, Johnson ME. Reducing agents affect inhibitory activities of compounds: results from multiple drug targets. *Anal Biochem.* 2012;423(1):46-53.
70. Tihonov MM, Kim VV, Noskov BA. Impact of a Reducing Agent on the Dynamic Surface Properties of Lysozyme Solutions. *J Oleo Sci.* 2016;65(5):413-8.
71. Trachootham D, Alexandre J, Huang P. Targeting cancer cells by ROS-mediated mechanisms: a radical therapeutic approach? *Nat Rev Drug Discov.* 2009;8(7):579-91.
72. Paravicini TM, Touyz RM. Redox signaling in hypertension. *Cardiovascular Research.* 2006;71(2):247-58.
73. Haigis MC, Yankner BA. The aging stress response. *Mol Cell.* 2010;40(2):333-44.
74. Singh A, Kukreti R, Saso L, Kukreti S. Oxidative Stress: A Key Modulator in Neurodegenerative Diseases. *Molecules.* 2019;24(8).
75. Plascencia-Villa G, Perry G. Preventive and Therapeutic Strategies in Alzheimer's Disease: Focus on Oxidative Stress, Redox Metals, and Ferroptosis. *Antioxid Redox Signal.* 2021;34(8):591-610.
76. Sbodio JI, Snyder SH, Paul BD. Redox Mechanisms in Neurodegeneration: From Disease Outcomes to Therapeutic Opportunities. *Antioxid Redox Signal.* 2019;30(11):1450-99.
77. Paulsen CE, Carroll KS. Cysteine-Mediated Redox Signaling: Chemistry, Biology, and Tools for Discovery. *Chemical Reviews.* 2013;113(7):4633-79.
78. Diao Y, Liu W, Wong CC, Wang X, Lee K, Cheung PY, et al. Oxidation-induced intramolecular disulfide bond inactivates mitogen-activated protein kinase kinase 6 by inhibiting ATP binding. *Proc Natl Acad Sci U S A.* 2010;107(49):20974-9.
79. Du X, Li Y, Xia YL, Ai SM, Liang J, Sang P, et al. Insights into Protein-Ligand Interactions: Mechanisms, Models, and Methods. *Int J Mol Sci.* 2016;17(2).
80. Ma G, Shan X, Wang S, Tao N. Quantifying Ligand-Protein Binding Kinetics with Self-Assembled Nano-oscillators. *Anal Chem.* 2019;91(21):14149-56.
81. Aykul S, Martinez-Hackert E. Determination of half-maximal inhibitory concentration using biosensor-based protein interaction analysis. *Anal Biochem.* 2016;508:97-103.
82. Zhang H, Holden-Wiltse J, Wang J, Liang H. A strategy to model nonmonotonic dose-response curve and estimate IC<sub>50</sub>. *PLoS One.* 2013;8(8):e69301.
83. Cheng HC. The power issue: determination of KB or Ki from IC<sub>50</sub>. A closer look at the Cheng-Prusoff equation, the Schild plot and related power equations. *J Pharmacol Toxicol Methods.* 2001;46(2):61-71.
84. Eble JA. Titration ELISA as a Method to Determine the Dissociation Constant of Receptor Ligand Interaction. *J Vis Exp.* 2018(132).
85. Gerecsei T, Chrenkó P, Kanyo N, Péter B, Bonyár A, Székács I, et al. Dissociation Constant of Integrin-RGD Binding in Live Cells from Automated Micropipette and Label-Free Optical Data. *Biosensors (Basel).* 2021;11(2).

86. Liu T, Marcinko TM, Vachet RW. Protein-Ligand Affinity Determinations Using Covalent Labeling-Mass Spectrometry. *J Am Soc Mass Spectrom.* 2020;31(7):1544-53.
87. Gomis-Tena J, Brown BM, Cano J, Trenor B, Yang P-C, Saiz J, et al. When Does the IC50 Accurately Assess the Blocking Potency of a Drug? *Journal of Chemical Information and Modeling.* 2020;60(3):1779-90.
88. Hafner M, Niepel M, Chung M, Sorger PK. Growth rate inhibition metrics correct for confounders in measuring sensitivity to cancer drugs. *Nat Methods.* 2016;13(6):521-7.
89. Cook PF. Kinetic studies to determine the mechanism of regulation of bovine liver glutamate dehydrogenase by nucleotide effectors. *Biochemistry.* 1982;21(1):113-6.
90. Samuel ELG, Holmes SL, Young DW. Processing binding data using an open-source workflow. *J Cheminform.* 2021;13(1):99.
91. Inkscape Available from: <https://inkscape.org>.
92. Huynh K, Partch CL. Analysis of protein stability and ligand interactions by thermal shift assay. *Curr Protoc Protein Sci.* 2015;79:28.9.1-.9.14.
93. Kazlauskas E, Petrauskas V, Paketuryte V, Matulis D. Standard operating procedure for fluorescent thermal shift assay (FTSA) for determination of protein-ligand binding and protein stability. *Eur Biophys J.* 2021;50(3-4):373-9.
94. Dumas P. Isothermal titration calorimetry in the single-injection mode with imperfect mixing. *Eur Biophys J.* 2022;51(1):77-84.
95. Salim NN, Feig AL. Isothermal titration calorimetry of RNA. *Methods.* 2009;47(3):198-205.
96. Bastos M, Velazquez-Campoy A. Isothermal titration calorimetry (ITC): a standard operating procedure (SOP). *Eur Biophys J.* 2021;50(3-4):363-71.
97. Di Trani JM, De Cesco S, O'Leary R, Plescia J, do Nascimento CJ, Moitessier N, et al. Rapid measurement of inhibitor binding kinetics by isothermal titration calorimetry. *Nat Commun.* 2018;9(1):893.
98. Stein JAC, Ianeselli A, Braun D. Kinetic Microscale Thermophoresis for Simultaneous Measurement of Binding Affinity and Kinetics. *Angew Chem Int Ed Engl.* 2021;60(25):13988-95.
99. Lopez-Mendez B, Baron B, Brautigam CA, Jowitt TA, Knauer SH, Uebel S, et al. Reproducibility and accuracy of microscale thermophoresis in the NanoTemper Monolith: a multi laboratory benchmark study. *Eur Biophys J.* 2021;50(3-4):411-27.
100. Al Hamoui D, Banni G, Nasreddine R, Fayad S, Colas C, Marchal A, Nehme R. Investigation of lipase-ligand interactions in porcine pancreatic extracts by microscale thermophoresis. *Anal Bioanal Chem.* 2021;413(14):3667-81.
101. Jerabek-Willemsen M, Wienken CJ, Braun D, Baaske P, Duhr S. Molecular interaction studies using microscale thermophoresis. *Assay Drug Dev Technol.* 2011;9(4):342-53.
102. Chang CA, Huang YM, Mueller LJ, You W. Investigation of Structural Dynamics of Enzymes and Protonation States of Substrates Using Computational Tools. *Catalysts.* 2016;6(6).
103. Hug S. Classical molecular dynamics in a nutshell. *Methods Mol Biol.* 2013;924:127-52.
104. Collier TA, Piggot TJ, Allison JR. Molecular Dynamics Simulation of Proteins. *Methods Mol Biol.* 2020;2073:311-27.
105. Fałat T, Platek B. Growth of intermetallic compound between indium-based thermal interface material and copper substrate: Molecular dynamics simulations. *Materials Science-Poland.* 2015;33.

106. QuikChange II Site-Directed Mutagenesis Kit (Agilent Technologies), Instruction manual Available from:  
<<http://www.chem.agilent.com/library/usermanuals/Public/200555.pdf>>
107. QuikChange Primer Design online software by Agilent Technologies.
108. XL1-Blue Supercompetent Cells (Agilent Technologies) Available from:  
<<https://www.agilent.com/cs/library/usermanuals/Public/200518.pdf>>
109. Nanodrop 2000c Available from:  
<<http://www.nanodrop.com/productnd2000coverview.aspx>>
110. Vagin AA, Teplyakov A. MOLREP: an automated program for Molecular Replacement. *Journal of Applied Crystallography*. 1997;30:1022-5.
111. Murshudov GN, Vagin AA, Dodson EJ. Refinement of macromolecular structures by the maximum-likelihood method. *Acta Crystallogr D Biol Crystallogr*. 1997;53(Pt 3):240-55.
112. Adams PD, Afonine PV, Bunkóczi G, Chen VB, Davis IW, Echols N, et al. PHENIX: a comprehensive Python-based system for macromolecular structure solution. *Acta Crystallogr D Biol Crystallogr*. 2010;66(Pt 2):213-21.
113. Lu C, Wu C, Ghoreishi D, Chen W, Wang L, Damm W, et al. OPLS4: Improving Force Field Accuracy on Challenging Regimes of Chemical Space. *J Chem Theory Comput*. 2021;17(7):4291-300.
114. Graphpad Prism 9 [
115. Williams CJ, Headd JJ, Moriarty NW, Prisant MG, Videau LL, Deis LN, et al. MolProbity: More and better reference data for improved all-atom structure validation. *Protein Sci*. 2018;27(1):293-315.
116. Lee B, Richards FM. The interpretation of protein structures: estimation of static accessibility. *J Mol Biol*. 1971;55(3):379-400.
117. Soundararajan M, Roos AK, Savitsky P, Filippakopoulos P, Kettenbach AN, Olsen JV, et al. Structures of Down syndrome kinases, DYRKs, reveal mechanisms of kinase activation and substrate recognition. *Structure*. 2013;21(6):986-96.
118. Ogawa Y, Nonaka Y, Goto T, Ohnishi E, Hiramatsu T, Kii I, et al. Development of a novel selective inhibitor of the Down syndrome-related kinase Dyrk1A. *Nat Commun*. 2010;1:86.
119. Tahtouh T, Elkins JM, Filippakopoulos P, Soundararajan M, Burgy G, Durieu E, et al. Selectivity, cocrystal structures, and neuroprotective properties of leucettines, a family of protein kinase inhibitors derived from the marine sponge alkaloid leucettamine B. *J Med Chem*. 2012;55(21):9312-30.
120. Anderson K, Chen Y, Chen Z, Dominique R, Glenn K, He Y, et al. Pyrido[2,3-d]pyrimidines: discovery and preliminary SAR of a novel series of DYRK1B and DYRK1A inhibitors. *Bioorg Med Chem Lett*. 2013;23(24):6610-5.
121. Falke H, Chaikuad A, Becker A, Loaëc N, Lozach O, Abu Jhaisha S, et al. 10-iodo-11H-indolo[3,2-c]quinoline-6-carboxylic acids are selective inhibitors of DYRK1A. *J Med Chem*. 2015;58(7):3131-43.
122. Wurzlbauer A, Rüben K, Gürdal E, Chaikuad A, Knapp S, Sippl W, et al. How to Separate Kinase Inhibition from Undesired Monoamine Oxidase A Inhibition-The Development of the DYRK1A Inhibitor AnnH75 from the Alkaloid Harmine. *Molecules*. 2020;25(24).
123. Rothweiler U, Stensen W, Brandsdal BO, Isaksson J, Leeson FA, Engh RA, et al. Probing the ATP-Binding Pocket of Protein Kinase DYRK1A with Benzothiazole Fragment Molecules. *Journal of Medicinal Chemistry*. 2016;59(21):9814-24.
124. Fukuda T, Ishiyama T, Katagiri T, Ueda K, Muramatsu S, Hashimoto M, et al. Discovery of DS42450411 as a potent orally active hepcidin production inhibitor: Design and

- optimization of novel 4-aminopyrimidine derivatives. *Bioorg Med Chem Lett*. 2018;28(20):3333-7.
125. Czarna A, Wang J, Zelencova D, Liu Y, Deng X, Choi HG, et al. Novel Scaffolds for Dual Specificity Tyrosine-Phosphorylation-Regulated Kinase (DYRK1A) Inhibitors. *J Med Chem*. 2018;61(17):7560-72.
126. Zheng M, Zhang Q, Zhang C, Wu C, Yang K, Song Z, et al. A natural DYRK1A inhibitor as a potential stimulator for  $\beta$ -cell proliferation in diabetes. *Clin Transl Med*. 2021;11(7):e494.
127. Henderson SH, Sorrell F, Bennett J, Hanley MT, Robinson S, Hopkins Navratilova I, et al. Mining Public Domain Data to Develop Selective DYRK1A Inhibitors. *ACS Medicinal Chemistry Letters*. 2020;11(8):1620-6.
128. Lechner C, Flaßhoff M, Falke H, Preu L, Loaëc N, Meijer L, et al. [b]-Annulated Halogen-Substituted Indoles as Potential DYRK1A Inhibitors. *Molecules*. 2019;24:4090.
129. Liu YA, Jin Q, Zou Y, Ding Q, Yan S, Wang Z, et al. Selective DYRK1A Inhibitor for the Treatment of Type 1 Diabetes: Discovery of 6-Azaindole Derivative GNF2133. *J Med Chem*. 2020;63(6):2958-73.
130. Kumar K, Wang P, Wilson J, Zlatanovic V, Berrouet C, Khamrui S, et al. Synthesis and Biological Validation of a Harmine-Based, Central Nervous System (CNS)-Avoidant, Selective, Human  $\beta$ -Cell Regenerative Dual-Specificity Tyrosine Phosphorylation-Regulated Kinase A (DYRK1A) Inhibitor. *J Med Chem*. 2020;63(6):2986-3003.
131. Lee Walmsley D, Murray JB, Dokurno P, Massey AJ, Benwell K, Fiumana A, et al. Fragment-Derived Selective Inhibitors of Dual-Specificity Kinases DYRK1A and DYRK1B. *Journal of Medicinal Chemistry*. 2021;64(13):8971-91.
132. Weber C, Sipos M, Paczal A, Balint B, Kun V, Foloppe N, et al. Structure-Guided Discovery of Potent and Selective DYRK1A Inhibitors. *J Med Chem*. 2021;64(10):6745-64.
133. Miyazaki Y, Kikuchi M, Umezawa K, Descamps A, Nakamura D, Furuie G, et al. Structure-activity relationship for the folding intermediate-selective inhibition of DYRK1A. *Eur J Med Chem*. 2022;227:113948.
134. Kaltheuner IH, Anand K, Moecking J, Düster R, Wang J, Gray NS, et al. Abemaciclib is a potent inhibitor of DYRK1A and HIP kinases involved in transcriptional regulation. *Nature Communications*. 2021;12(1):6607.
135. Demuro S, Sauvey C, Tripathi SK, Di Martino RMC, Shi D, Ortega JA, et al. ARN25068, a versatile starting point towards triple GSK-3 $\beta$ /FYN/DYRK1A inhibitors to tackle tau-related neurological disorders. *European Journal of Medicinal Chemistry*. 2022;229:114054.